frontiers | Frontiers in Detector Science and Technology

TYPE Original Research
PUBLISHED 07 January 2025
DOI 10.3389/fdest.2024.1480975

A review of NEST models for liquid xenon and an exhaustive comparison with other approaches

M. Szydagis[1]*, J. Balajthy[2,3], G. A. Block[1,4,5], J. P. Brodsky[6], E. Brown[4], J. E. Cutter[2,7], S. J. Farrell[8], J. Huang[2,9], A. C. Kamaha[1,10], E. S. Kozlova[11,12], C. S. Liebenthal[8], D. N. McKinsey[13,14], K. McMichael[4], R. McMonigle[1], M. Mooney[15], J. Mueller[15], K. Ni[9], G. R. C. Rischbieter[1,16,17]*, K. Trengove[1,10], M. Tripathi[2], C. D. Tunnell[8], V. Velan[13], S. Westerdale[18], M. D. Wyman[1], Z. Zhao[9] and M. Zhong[9]

[1]Department of Physics, University at Albany, State University of New York, Albany, NY, United States, [2]Department of Physics, University of California Davis, Davis, CA, United States, [3]Sandia National Laboratories, Livermore, CA, United States, [4]Department of Physics, Applied Physics and Astronomy, Rensselaer Polytechnic Institute, Troy, NY, United States, [5]Department of Physics and Astronomy, University of New Mexico, Albuquerque, NM, United States, [6]Lawrence Livermore National Laboratory, Livermore, CA, United States, [7]Deepgram, Mountain View, CA, United States, [8]Department of Physics and Astronomy, Rice University, Houston, TX, United States, [9]Department of Physics, University of California San Diego, La Jolla, CA, United States, [10]Department of Physics and Astronomy, University of California Los Angeles, Los Angeles, CA, United States, [11]Institute for Theoretical and Experimental Physics Named by A.I. Alikhanov of National Research Centre “Kurchatov Institute”, Moscow, Russia, [12]Moscow Engineering Physics Institute (MEPhI), National Research Nuclear University, Moscow, Russia, [13]Lawrence Berkeley National Laboratory, Berkeley, CA, United States, [14]Department of Physics, University of California Berkeley, Berkeley, CA, United States, [15]Department of Physics, Colorado State University, Fort Collins, CO, United States, [16]Department of Physics, University of Michigan, Ann Arbor, MI, United States, [17]Physik-Institut, University of Zürich, Zürich, Switzerland, [18]Department of Physics and Astronomy, University of California Riverside, Riverside, CA, United States

This paper discusses the microphysical simulation of interactions in liquid xenon, the active detector medium in many leading rare-event searches for new physics, and describes experimental observables useful for understanding detector performance. The scintillation and ionization yield distributions for signal and background are presented using the Noble Element Simulation Technique (NEST), a toolkit based on experimental data and simple empirical formulas, which mimic previous microphysics modeling but are guided by data. The NEST models for light and charge production as a function of the particle type, energy, and electric field are reviewed, along with models for energy resolution and final pulse areas. NEST is compared with other models or sets of models and validated against real data, with several specific examples drawn from XENON, ZEPLIN, LUX, LZ, PandaX, and table-top experiments used for calibrations.

KEYWORDS

WIMPs, dark matter, direct detection, liquid Xenon, simulations / models

Check for updates

OPEN ACCESS

EDITED BY
Diego Gonzalez-Diaz,
University of Santiago de Compostela, Spain

REVIEWED BY
Aleksey Bolotnikov,
Brookhaven National Laboratory (DOE),
United States
Carlos Ourivio Escobar,
Fermi National Accelerator Laboratory (DOE),
United States

*CORRESPONDENCE
M. Szydagis,
✉ mszydagis@albany.edu
G. R. C. Rischbieter,
✉ rischbie@umich.edu

RECEIVED 14 August 2024
ACCEPTED 04 December 2024
PUBLISHED 07 January 2025

CITATION
Szydagis M, Balajthy J, Block GA, Brodsky JP, Brown E, Cutter JE, Farrell SJ, Huang J, Kamaha AC, Kozlova ES, Liebenthal CS, McKinsey DN, McMichael K, McMonigle R, Mooney M, Mueller J, Ni K, Rischbieter GRC, Trengove K, Tripathi M, Tunnell CD, Velan V, Westerdale S, Wyman MD, Zhao Z and Zhong M (2025) A review of NEST models for liquid xenon and an exhaustive comparison with other approaches.
Front. Detect. Sci. Technol 2:1480975.
doi: 10.3389/fdest.2024.1480975

1 Introduction

For the past 15+ years, leading results in dark matter direct detection searches have been obtained from detectors based on the principle of the dual-phase Time Projection Chamber (TPC) using a liquefied noble element as the detection medium (Baudis, 2018). Liquid xenon (LXe) TPCs, in particular, have produced the most stringent cross-section constraints for Spin-Independent (SI) and neutron Spin-Dependent (SD) interactions between Weakly Interacting Massive Particles (WIMPs) and xenon nuclei. More recently, the use of LXe has also led to WIMP limits using different Effective Field Theory (EFT) operators for mass-energies above $O(5\text{ GeV})$ (Akerib et al., 2021a). EFT extends the set of allowable operators beyond the standard SI and SD interactions and includes searches at higher nuclear recoil energies. Unrelated to dark matter, electron recoil searches up to the MeV regime have set strict constraints on $0\nu\beta\beta$ decay (Anton et al., 2019) and led to observations of double e^- capture (Aprile et al., 2019a). XENONnT and PandaX have recently illustrated the potential for precision measurements of ^{8}B (Aprile, 2024a; Bo, 2024).

To interpret results from past, present, and future experiments, a reliable Monte Carlo (MC) simulation is required. Recent works have demonstrated the utility of NEST, the cross-disciplinary, detector-agnostic MC software reviewed in this study (Akerib et al., 2021b; Yan et al., 2021; Aprile et al., 2021), for a variety of active detector materials: LAr (Caratelli, 2022; Abud et al., 2023; Westerdale, 2024) and GXe, especially LXe. As the multi-tonne-scale TPCs have commenced data collection (Aalbers et al., 2023; Yan et al., 2021; Aprile et al., 2021), improved MC techniques will not only assist in limit setting but also be essential for determining the mass and cross section of dark matter particles in the event of a WIMP discovery. In either scenario or for the design of a new TPC, predictions of performance are needed on key metrics like the fundamental scintillation light and ionization charge yields for LXe, which is the focus of this work. NEST v2.4 is its default model; different versions are specified as needed. This manuscript is a technical overview of updates to NEST, including new models and comparisons. More pedagogical reviews of the models and related physics are available in the studies of Szydagis et al. (2011) and Szydagis et al. (2021a).

Section 2.1 presents the mean scintillation and ionization yields of electronic recoil (ER) backgrounds, along with comparisons to experimental data. These serve as the basis for the ER background (BG) models in Xe-based dark matter detectors. Section 2.2 summarizes the methods for varying these mean yields to model realistic fluctuations, with variations in the total number of quanta (light and charge) produced. Section 2.3 focuses on the yields of nuclear recoils (NRs) and their fluctuations. These form the foundation for the signal model in an LXe-based dark matter search, as well as for NR backgrounds (such as those from fast neutron scattering and coherent elastic neutrino-nucleus scattering, CEνNS). Lastly, Section 3 compares NEST's modeling of mean yields (Sections 2.1 and 2.3) with past and present approaches in the existing literature, including some based on first-principles methods, before the conclusion. The strengths and weaknesses of the different approaches are summarized, underscoring NEST's ability to phenomenologically model data across a broad range of energies and electric fields.

2 Microphysics modeling evaluation

The NEST model choices were justified earlier by Szydagis et al. (2021a) and in the references therein, but they are re-evaluated in this study more comprehensively with newer and more extensive datasets. NEST is openly shared, allowing for regular re-evaluation using the latest calibrations (Szydagis, 2020). Although such data often provide relative light and charge yields, these can be converted to absolute yields if the detector gains are calculable, known as g_1 and g_2 for these respective yields. The light yield gain, g_1, is the primary photon detection efficiency, while the charge gain, g_2, is the average signal size per e^- escaping the interaction site. Uncertainties in these gains are a significant source of systematic error, but newer data from higher-quality calibrations help mitigate this issue. Combining calibration data ranging from <1 keV to >1 MeV energy, NEST predicts the shapes of primary scintillation and ionization yields as functions of energy, E, and drift electric field, $\mathcal{E}$, for different particle interaction types (Conti et al., 2003). The status of the NEST modeling of these shapes is shown in Figure 1.

2.1 Electronic recoils (beta, gamma, and X rays)

NEST begins with a model of the total yield, summing the vacuum ultraviolet (VUV) scintillation photons and ionization electrons produced. IR photons are not included as their yield in LXe is lower by a factor of ~4 (Bressi et al., 2001), and their wavelength is beyond the sensitivity of most photon sensors commonly used in dark matter experiments. The work function, W_q, for the production of quanta depends only on the density, determined using a linear fit based on data collected by Aprile et al. (2008) across different phases (see also Supplementary Appendix SA):

$$W_q\ [eV] = 21.94 - 2.93\rho = \frac{W_i}{1 + N_{ex}/N_i}. \tag{1}$$

Here, ρ is the mass density in units of g/cm^3. LXe TPCs typically operate at temperatures of 165–180 K and pressures of 1.5–2 bar(a), leading to $\rho \approx 2.9$ g/cm^3 and resulting in a W_q value between 13 and 14 eV [Equation 1, with discrepant values discussed by Szydagis et al. (2021b)]. The exciton–ion ratio or N_{ex}/N_i relates W_q to the work function for ionization, W_i, which was defined for the charge yields. Moreover, N_{ex}/N_i determines the pre-recombination (of e^-s with ions) split of quanta into light and charge (see Supplementary Appendix SA, where ρ dependence is explained):

$$N_{ex}/N_i = (0.0674 + 0.0397\rho) \times \text{erf}\,(0.05E), \tag{2}$$

where E is the deposited energy in keV for a β interaction or Compton scatter and "erf" refers to the error function. Here, the ρ dependence is based again on Aprile et al. (2008), while the E dependence comes from reconciling Doke et al. (2002); Akerib et al. (2016a); and Lin et al. (2015), given the lines of evidence that light yield approaches 0 as energy E decreases, with lower-E data sets favoring both less recombination and smaller N_{ex}/N_i. Ionization electrons can recombine with Xe atoms or escape entirely from the interaction site. Therefore, the number of photons N_{ph} is not simply

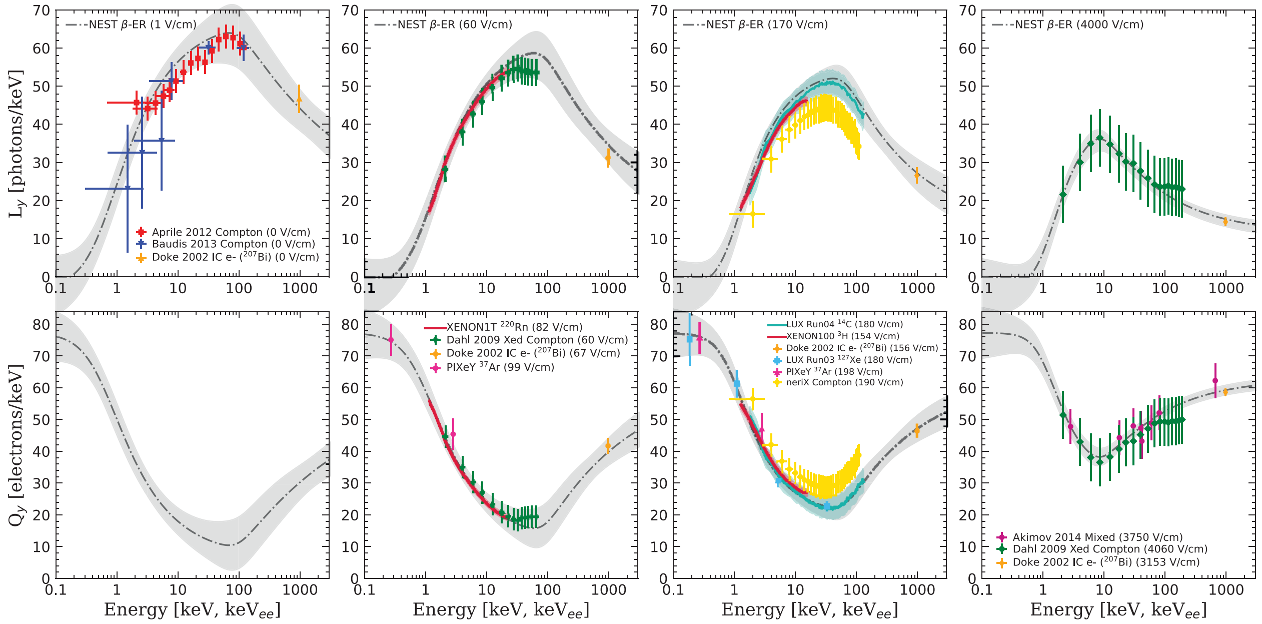

FIGURE 1
β electron recoil (ER) L_y (top row) and Q_y (bottom row) vs. energy E. Different fields $\mathcal{E}$ are represented from 0 V/cm (left column) to the highest fields for which data exist at multiple Es, ~3–4 kV/cm (right column). More datasets exist, all of which are utilized to inform NEST, but these are selected as representative examples of the lowest and highest $\mathcal{E}$s and lowest and highest Es, from sub-keV to 1 MeV across different types of experiments (Aprile et al., 2012; Baudis et al., 2013; Doke et al., 2002; Aprile et al., 2019b; Dahl, 2009; Boulton et al., 2017; Akerib D. et al., 2019; Aprile et al., 2018a; Akerib et al., 2017a; Goetzke et al., 2017; Akimov et al., 2014). MC lines are black-dashed with gray 1σ error bands. Newer results, *e.g.*, XENON1T's ^{220}Rn calibration, illustrate the predictive power of NEST using the latest β model, which stems largely from ^{14}C decays (Akerib D. et al., 2019; Akerib et al., 2020a).

equal to N_{ex}, providing an anti-correlation between the observed light and charge yields; this motivates the use of both charge and light to measure the energy, $E = W_q\,(N_{ph} + N_{e^-})$ (Szydagis et al., 2021a):

$$N_{ph} = N_{ex} + r(E,\mathcal{E},\rho)N_i = \mathrm{S1}/g_1 \text{ and}$$
$$N_{e^-} = [1 - r(E,\mathcal{E},\rho)]N_i = \mathrm{S2}/g_2, \quad (3)$$

where r is the recombination probability for e^--ion pairs depending on E, $\mathcal{E}$, and ρ, as well as the particle and interaction type, and S1 and S2 are the experimental observables. Typical values for g_1 are ~0.1 but $O(10)$ for g_2 due to secondary (gas) scintillation (g_2 is 0.5–1 in single-phase TPCs). The light and charge yields per unit energy are traditionally quoted in experiment, defined as $L_y \equiv N_{ph}/E$ and $Q_y \equiv N_{e^-}/E$, respectively.

Q_y is modeled first; L_y is set by W_q and subtraction:

$$N_q \equiv N_{ex} + N_i = N_{ph} + N_{e^-} = E/W_q, \text{ where}$$
$$N_{e^-} = Q_y E, \text{ and } N_{ph} = N_q - N_{e^-}, \quad (4)$$

where N_q is the total number of quanta. This procedure leverages the greater reliability of S2 measurements compared to S1 for lower E, as explained by Akerib et al. (2017a) and Szydagis et al. (2021a). Q_y in the ER model is a sum of two sigmoids:

$$Q_y(E,\mathcal{E}) = m_1(\mathcal{E}) + \frac{m_2 - m_1(\mathcal{E})}{\left[1+\left(\frac{E}{m_3(\mathcal{E})}\right)^{m_4(\mathcal{E})}\right]^{m_9}} + m_5(\mathcal{E}) - \frac{m_5(\mathcal{E})}{\left[1+\left(\frac{E}{m_7(\mathcal{E})}\right)^{m_8}\right]^{m_{10}(\mathcal{E})}}, \quad (5)$$

with m_1 serving as the minimum field-dependent charge yield. m_2 determines the low-E behavior, and m_7 controls the field dependence at high energies. The individual m_i values are summarized in Supplementary Appendix SB (with Akerib et al. (2020a) providing more details). Although empirical, the first (left, $m_1 + \cdots$) and second (right, $m_5 - \cdots$) sigmoids of Equation 5 capture the qualitative behavior of two first-principles options, respectively: the Thomas–Imel box model at low energies (Thomas and Imel, 1987) and Doke-modified Birks' law at higher energies (Doke et al., 1988). Between ~15 keV and the energy of a minimally ionizing particle (MIP) within Xe (approximately 1 MeV), a track shape is described as cylindrical by Doke for modeling the recombination, and dE/dx decreases with increasing E. The recombination probability r decreases as energy E increases, reducing the ratio of L_y to Q_y (Szydagis et al., 2022; Szydagis et al., 2011; Berger et al., 2005). Below ~15 keV, deposits are more amorphous, and straight 1-D track lengths become ill-defined: r and L_y increase with the 3-D ionization density and the energy as dE/dx increases with E.

A Thomas–Imel approach historically uses E and models energy deposits within symmetric boxes or spheres, while the

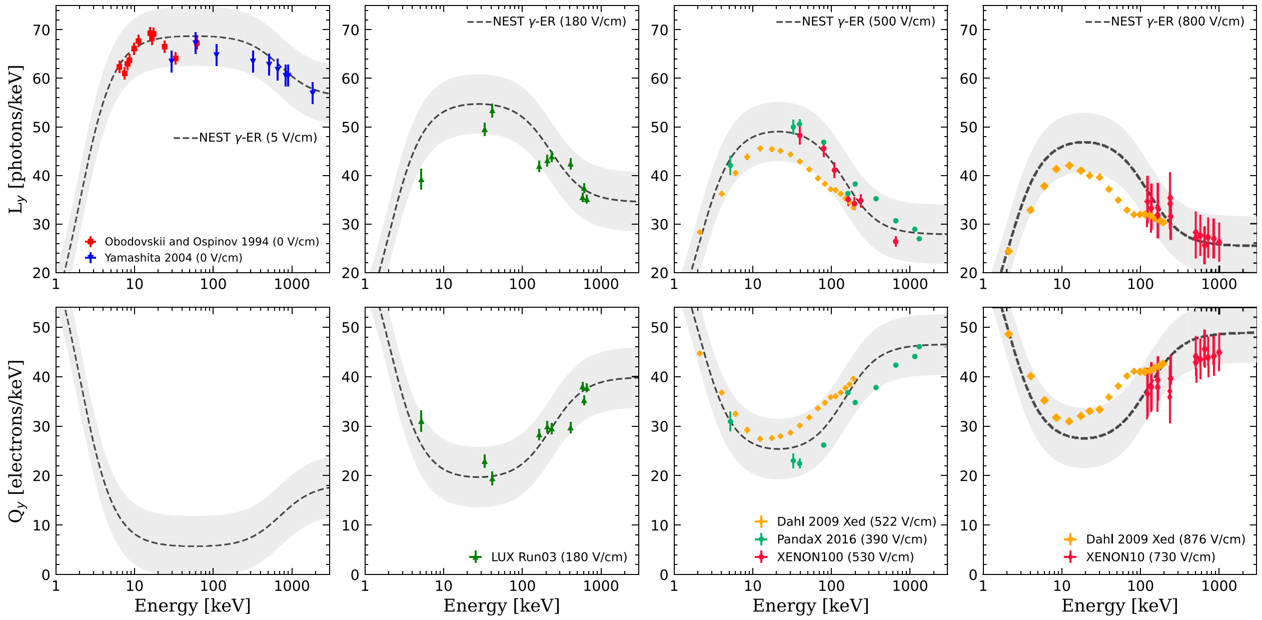

FIGURE 2
γ ER L_y (top row) and Q_y (bottom) vs. E at $\mathcal{E} = 0$ (left) to nearly 10^3 V/cm (right). Before β calibrations were common, photoabsorption peaks from monoenergetic γs were used (Obodovskii and Ospanov, 1994; Yamashita et al., 2004; Akerib et al., 2017b; Dahl, 2009; Tan et al., 2016; Aprile et al., 2010; Aprile et al., 2011). At sufficiently high E, L_y is higher and Q_y is lower than that in Figure 1 as some unresolvable multiple scattering occurs, treated as single scattering in NEST (Szydagis et al., 2013). Multiple lower-E and higher-dE/dx vertices are "averaged over." Low fields again approximate 0 V/cm, when NEST becomes singular. As in other plots, gray 1σ bands are driven by data errors, model shape constraints (sigmoidal), and monotonic $\mathcal{E}$ dependence. LUX L_y points, but not Q_y, seem systematically low due to a different W_q applied, with LUX assuming 13.7 eV (no ρ dependence). Dahl datasets exhibit different shapes due to being mixtures of Compton scatters and photoabsorption.

Doke/Birks' law uses dE/dx and assumes long tracks (cylinders). The former will exhibit r (and therefore L_y) only increasing with energy, while the latter will usually exhibit it decreasing, with Q_y anti-correlated again.

The recombination fraction or probability, r, is found retroactively in recent NEST versions after fitting to Q_y per Equation 5, chosen for matching both the box and Birks models. Using Equation 2 as a constraint avoids the degeneracy of this r with N_{ex}/N_i, with the sum $N_{ex} + N_i$ (also equal to $N_{ph} + N_{e^-}$) already constrained by Equations 1, 4—the former determines W_q, and the latter determines total quanta N_q based on W_q. Any change in W_q (one work function averaging over individual work functions for photon and electron production) should change L_y and Q_y equally, preserving both their shapes in both energy and field (Anton et al., 2020).

Figure 1 summarizes both L_y and Q_y for βs and Compton scattering ERs from both data and NEST, with NEST using typical LXe operating conditions of $\rho = 2.89$ g/cm^3 ($T = 173$ K and $P = 1.57$ bar). The non-monotonic energy dependence is obvious. Meanwhile, L_y decreases from left to right (top), and Q_y correspondingly increases (bottom) as the field increases, suppressing recombination at a fixed N_q. However, even at $\mathcal{E} = 0$, there exists a "phantom" Q_y, likely caused by an extreme delay in recombination, as explained by Doke et al. (2002) and Szydagis et al. (2021a); this is unobservable, except via long S1 integration times, and by noting that L_y vs. energy maintains the same shape at all fields, even at 0. This implies a continuous change in L_y as $\mathcal{E} \to 0$. Non-zero fields standing in for 0 represent residual stray fields in a detector and/or inherent fields of Xe atoms (Szydagis et al., 2013).

The absorption of any high-energy photon, a γ or x-ray, is modeled as β interactions and Compton scatters but with unique m_i (Figure 2) to capture sub-position-resolution multiple scatters and distinct dE/dx. L_y is mostly lower and Q_y is higher for βs, as explained within the Figure 2 caption. Although it might be possible to merge the γ and β models by relying on differences in dE/dx, γs are treated independently at present. Supplementary Appendix SB lists the β and γ model parameters, in addition to those for NR models.

2.2 Yield fluctuations

Energy resolution typically refers to Gaussian spreads (σ or FWHM) of monoenergetic peaks from high-energy γ-ray photoabsorption, but this is also relevant to lower energies in WIMP searches. The smearing of continuous ER spectra can drive an increase in signal-like background events. However, to understand statistical limitations for high-level parameters like monoenergetic-peak σs or background discrimination, we must start with lower-level parameters that underlie all the relevant stochastic processes involved. This modeling is discussed in depth by Szydagis et al. (2021a), but portions relevant to this work are summarized in this section, culminating in a subsection enumerating the practical steps taken within the NEST code on GitHub.

2.2.1 Total quanta: correlated fluctuations

Realistic smearing of mean yields begins with a Fano-like factor, F_q, applied to the total quanta, N_q, prior to differentiation into N_{ex} and N_i. It is labeled as Fano-like as it does not follow the strict sub-Poissonian definition (Doke et al., 1976). F_q may exceed 1, but it is still used in the usual definition of the standard deviation of N_q, utilized for decades by Xe experiments to fit their data on combined E (N_{ph} and N_{e-}) scale resolution:

$$\sigma_q = \sqrt{F_q \langle N_q \rangle}, \tag{6}$$

where F_q is defined for light and charge together as

$$F_q = 0.13 - 0.030\rho - 0.0057\rho^2 + 0.0016\rho^3 + \delta_F \sqrt{\langle N_q \rangle}\sqrt{\mathcal{E}}. \tag{7}$$

The first part of Equation 7 is a spline of data (Aprile et al., 2008) from gas, liquid, and solid. The constant 0.13 represents the theoretical value of the Xe Fano factor, following the traditional definition ($F_q < 1$). $O(0.1)$ matches NEXT gas data on N_{e-} (Alvarez et al., 2013) and Biagi's Degrad work. The second part of Equation 7 is only for liquid and is data-driven, where $\delta_F = 0.0015$ for LXe but is identically 0 for gaseous Xe. The $\sqrt{\langle N_q \rangle}$ term is included in order to match the data at MeV scales (*e.g.*, for $0\nu\beta\beta$ searches). Such results did not achieve the theoretical minimum in energy resolution even when reconstructing N_q, utilizing both channels of information (light and charge), instead of only a single channel. This was true even for the cases where the noise was allegedly subtracted or modeled (Delaquis et al., 2018; Aprile et al., 2020a). As Q_y increases with $\mathcal{E}$, the combined E resolution improves. However, the improvement is smaller than naïvely predicted, requiring the $\sqrt{\mathcal{E}}$ term in F_q to match the data (Aprile et al., 2007; Aprile et al., 1991).

There are many possible explanations for F_q becoming $\gg 1$ as E or $\mathcal{E}$ changes. W_q may need to be replaced with separate W_{ex} and W_i for the excitation and ionization processes (both inelastic scattering), respectively, and then further subdivided into different values that depend on the e^- energy shell. Lastly, elastic scattering of orbital e^-s may play a role. These mechanisms are discussed by Platzman (1961), but explicit Fano-factor variations can be found in Szydagis et al. (2021a). In NEST, a Gaussian smearing, constrained to be non-negative, is applied to N_q with a width defined by Equation 6: $N_q = G[\langle N_q \rangle, \sigma_q]$. A binomial distribution then divides quanta into excitons versus ions.

2.2.2 Anti-correlated excitation and recombination fluctuations

F_q drives resolution on a combined E scale, but such a scale is more relevant for monoenergetic peaks than dark matter searches (Dahl, 2009; Szydagis et al., 2021a). "Recombination fluctuations," however, describe the redistribution of N_{ph} and N_{e-} caused by widths associated with the means of Equations 3, 4. Often conflated with excitation fluctuations (Equation 2), these are all fundamental and do not originate from detector effects (Aprile at al., 2011; Akerib et al., 2017b); they constitute one of the key factors for the characterization of ER discrimination (Dobi, 2014). Moreover, they are not binomial, despite recombination (or escape) appearing to be a binary decision. Potential explanations for this phenomenon include other energy loss mechanisms, or other effects that break the independence of draws, for instance, δ-ray production (as observed at different energies in both Ar and Xe (Amoruso et al., 2004; Thomas et al., 1988)), the statistics of columnar recombination (Nygren, 2013), and short-lived clustering of Xe dimers (Davis et al., 2016).

While it remains unclear which explanation is correct, NEST proceeds with a fully empirical approach to simply model what is observed in data; following the works by Akerib et al. (2017b) and Akerib et al. (2020a) closely, NEST defines recombination variance as follows:

$$\begin{aligned}
&\sigma_r^2 = \langle r \rangle (1 - \langle r \rangle) N_i + \sigma_p^2 N_i^2, \text{ where} \\
&\sigma_r \approx \sigma_{N_{e^-}} \approx \sigma_{N_{ph}} \left(\text{for small } F_q\right), \\
&\sigma_p = A(\mathcal{E}) e^{\frac{-(\langle y \rangle - \xi)^2}{2\omega^2}} \left[1 + \text{erf}\left(\alpha_p \frac{\langle y \rangle - \xi}{\omega\sqrt{2}}\right)\right], \text{ and the e}^- \text{ fraction} \\
&y = N_{e^-}/N_q \text{ and } \langle y \rangle = Q_y W_q.
\end{aligned} \tag{8}$$

$\langle r \rangle (1 - \langle r \rangle) N_i$ in σ_r follows the binomial expectation of $\sigma_r \propto \sqrt{N_i}$. The σ_p term leads to $\sigma_r \propto N_i$, as proposed by Dobi (2014). σ_p is a skewed Gaussian (on the third line) with field-dependent amplitude, A, varying from 0.05 to 0.1, as needed to simulate the spectral broadening of ER with higher drift electric field (Akerib et al., 2020a; Akerib et al., 2020b). In NEST versions $<$ 2.1, σ_p was simulated as a constant, similar in value to A, but this was found to be inadequate for capturing the full behavior of recombination fluctuations (Akerib et al., 2017b).

σ_p's dependent variable was chosen to be the mean electron fraction $\langle y \rangle$ for simplicity as it is closely related to $1 - \langle r \rangle$. Recombination probability, defined within Equation 3, is degenerate with N_{ex}/N_i, while y is directly measurable. It can be written in terms of r: $y = (1 - r)/(1 + N_{ex}/N_i)$ (Dahl, 2009). Non-binomial fluctuations decrease as y approaches 0 or 1, causing σ_p to vanish. ξ, ω, and α_p are the centroid, width, and skew of σ_p, respectively. Default NEST values determining the width and skewness of σ_p are $\omega = 0.2$ and $\alpha_p = -0.2$, respectively (future work may recast σ_r entirely in terms of y not just σ_p).

A skew centroid $\xi \approx 0.4$–0.5 was found based on β and γ datasets. The types of datasets included continuous spectra and monoenergetic-peak energy resolutions, both at multiple fields and energies (Dahl, 2009; Aprile et al., 2011; Dobi, 2014). ξ's value depends on which datasets are used and which other parameters are fixed. A ξ near 0.5 leads to a maximum in σ_p (within σ_r) near $y = 0.5$, as would occur within a regular binomial distribution. The asymmetric shape σ_p is motivated by observations of recombination fluctuations at lower values of y (low field, high energy) compared to higher values of y (high field, low energy) (Rischbieter, 2022; Dobi, 2014; Akerib et al., 2020a).

Longer, less technical descriptions of all the steps in Section 2.2.2 can be found in the studies by Akerib et al. (2020a) and Rischbieter (2022).

2.2.3 Recombination skewness

We note that the skewed Gaussian $\sigma_p(y)$ must not be conflated with E and $\mathcal{E}$-dependent skew defined in Section IVB of Akerib et al. (2020b) as α_r; the skew in that study represented the observed asymmetry of the resultant charge yields. NEST uses α_r from Equation 13 in Akerib et al. (2020b) to smear the mean N_{e^-},

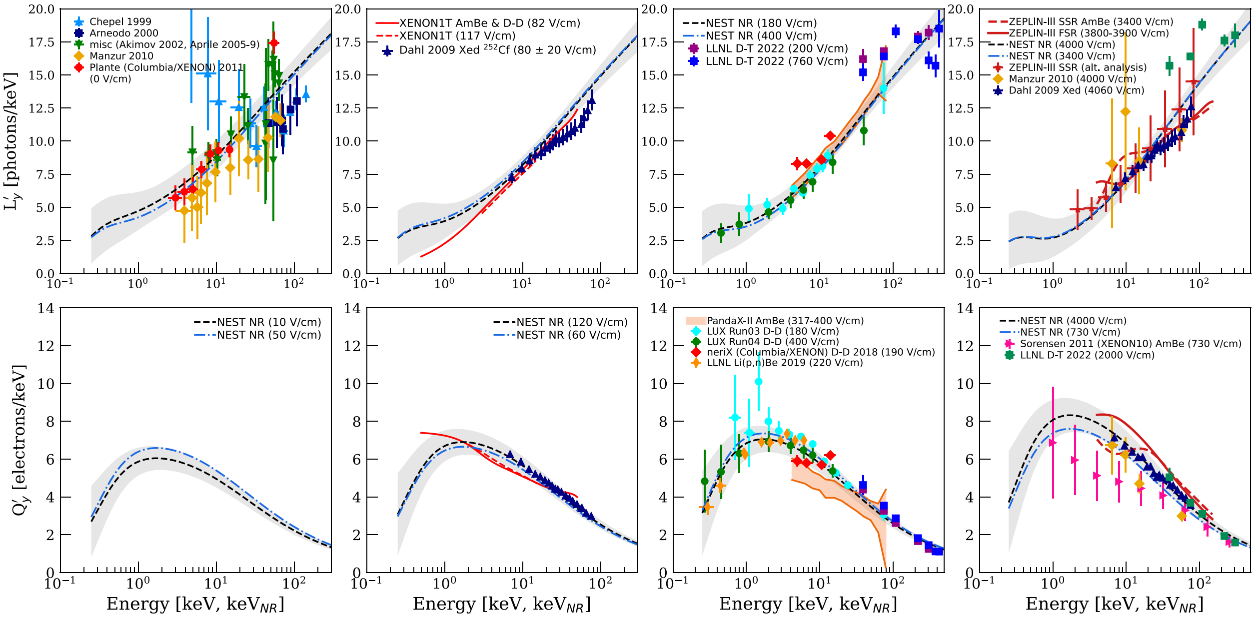

FIGURE 3
NR L_y' (top) and Q_y' (bottom) vs. E, from $\mathcal{E} = 0$ V/cm at left to the highest $\mathcal{E}$ for which data exist at right (Aprile et al., 2019b; Dahl, 2009; Chepel, 1999; Arneodo et al., 2000; Akimov et al., 2002; Aprile et al., 2005; Aprile et al., 2009; Manzur et al., 2010; Plante et al., 2011; Aprile et al., 2017; Yan et al., 2021; Akerib, 2016; Akerib et al., 2017c; Huang, 2020; Akerib, 2022; Aprile et al., 2018b; Lenardo et al., 2019; Horn et al., 2011; Sorensen, 2011a). Newer works from XENON1T and PandaX were not included in fits (yet agree at the 1–2σ level). NEST lines are blue and black at similar $\mathcal{E}$s. Uncertainties in NEST increase as $E \to 0$ or ∞ as the amount of data decreases at each extreme. $\mathcal{E}$ dependence is weaker compared with ER (Figure 2). Summing L_y' and Q_y' results in a power law, not a constant (ER), while $N_q' < N_q$ (Sorensen and Dahl, 2011; Szydagis et al., 2021a). For systematically offset datasets, our fit can average them if they share the same qualitative trend. Discrepant results sharing the same trend point toward a systematic offset in the S1 and/or S2 gains, with S1 most affected by the secondary-PE effect (Faham et al., 2015) and S2 affected by assuming 100% e^- extraction prior to more recent measurements (Edwards et al., 2018; Xu et al., 2019). Only Chepel 1999 L_y (upper left) is excluded from the fits used to tune NEST. As NR dE/dx decreases with decreasing E, e^- escape probability increases, causing L_y' to decrease (L_y''s shape is also determined by the $\mathcal{L}$-factor). For Q_y', there is a maximum value because the $\mathcal{L}$-factor decreases and $(1 - r)$ increases at different rates as $E \to 0$. In contrast to the study by Szydagis et al. (2021a), where the focus was $\mathcal{L}$, we separate L_y' and Q_y' in this study. Although errors imply no field dependence, when data are taken in one detector at many fields, an increasing Q_y' value (decreasing L_y') with field is clear (Dahl, 2009).

while α_p controls the variance of recombination fluctuations, σ_r, as described in Equation 8.

A positive α_r value can lead to better background discrimination than expected for a WIMP search that uses LXe. Weak rejection was expected due to the recombination fluctuations being greater (worse) than binomial, but positive α_r will shift ER events preferentially away from NR (more Q_y). This has already been observed by Akerib et al. (2020b).

2.2.4 Uncorrelated fluctuations: detector effects (known and unknown)

Lastly, while the simulated σ_q widths predict correlated changes in S1 (L_y) and S2 (Q_y) and σ_r leads to an anti-correlated change, uncorrelated noise also exists, affecting S1 and S2 independently. S1 and S2 gains are understood sources, assuming position-dependent light collection and field non-uniformities are taken into account. Unknown sources are modeled with a Gaussian smearing proportional to the pulse areas (Szydagis et al., 2021b). A quadratic term may be necessary at the MeV scale (Davis et al., 2016). ER and NR are equally affected by any detector effects (known/unknown). The final E resolutions vs. E are observed for ER, NR, or both (Akerib et al., 2021b; Szydagis et al., 2021b), supplementing the validation of means in Figures 1–3 with their vetting of fluctuations. The scale of the unknown detector effects across experiments is 1%–10% (Szydagis et al., 2021b; Szydagis et al., 2021a; Aalbers et al., 2024) (for S2s and non-integer forms of S1s) but effectively 0% for a spike count of S1 photons. For further details, refer to Supplementary Appendix SA.

2.2.5 Computational implementation

NEST is publicly available as a GitHub repository, which includes the source code, interface scripts, and examples. It is C++-based but can be run with dedicated scripts using either C++ or Python, both of which are available in the repository. These can be used to generate expectation values of yields and their fluctuations for different detectors using Xe or Ar. The step-by-step procedure that NEST follows to perform these tasks is summarized below:

- F_q is used to determine σ_q for a normal distribution of total (initially undifferentiated) ER quanta, which can be considered "correlated noise" because, in this case, N_{ph} and N_{e-} increase and decrease together [**Eq A1** (Aprile, 2024b)]. Two distinct Fs exist for NR N_{ex} and N_i, breaking the correlation (Section 2.3).
- ER quanta are differentiated (N_{ex} and N_i) using a binomial distribution [**Eq A2** (Aprile, 2024b)], approximated as normal for computational speed, using the same Box-Muller

algorithm as in the first step above. Any non-binomial/ non-Gaussian fluctuation at this stage is essentially degenerate with the next step.
- A normal or skew-normal [**Eq 8–12** (Akerib et al., 2020b)] in N_{e-} capped at N_q (minimum of 0) enforces the anti-correlated fluctuation of N_{ph} versus N_{e-}. This step was previously mismodeled by uncorrelated Fano factors. The variance σ_r^2 has components proportional to both N_i ("binomial style") and N_i^2 (data-driven).

Two more lists cover detector specifics for S1 and S2, closely following Supplementary Appendix SC of Aprile (2024b). First, S1 comprises the following:

- S1.1 A binomial distribution with probability g_1 (3-D spatially varying) determines the fraction of N_{ph} successfully detected by photo-sensors; g_1 represents the product of geometric × quantum efficiencies.
- S1.2 Single photo-electrons in sensors are modeled by zero-truncated Gaussians of sensor-specific width. Spike counting is emulated using artificially reduced width but non-zero for matching real data.
- S1.3 An if-else structure determines whether a second photoelectron is produced due to the secondary PE effect. This step and S1.2 are Gaussian-approximated at high E in the "hybrid" mode or any E in the "parametric" mode.
- S1.4 Geant4 (G4), Chroma, OptiX, or some other ray-tracer, or NEST's built-in analytic-approximation ability simulates photon arrival times at S1 sensors and dictates whether a sufficient number of photons were detected in MC with above-threshold (experiment DAQ-specific) pulse areas, based upon stages S1.2 and S1.3 above.

The procedure to model the charge signal or S2 is more intricate, especially in a two-phase experiment:

- S2.1 Electrons (numbered N_{e-}) diffuse both transversely and longitudinally as they drift at a drift speed determined by the liquid's field but also influenced by factors such as density, temperature, and pressure (the same applies to diffusion "constants"). Data-driven functions exist for all these phenomena in NEST.
- S2.2 An electron survival fraction is set by an exponential function depending on the originating depth in a detector and a characteristic electron MFP. It is used as the probability in a binomial distribution.
- S2.3 Another binomial distribution is utilized to find how many electrons survive extraction from the liquid to the gas. The efficiency is a function of the gas field $\mathcal{E}_g$ between the liquid/gas boundary and gate grid. NEST offers many options of asymptotic (1 at infinite $\mathcal{E}_g$) function based on the past data.
- S2.4 Each extracted electron produces Y_{e-} S2 photons based on the parameterization described by Chepel and Araújo (2013) depending on $\mathcal{E}_g$, gas ρ, and the gap between the liquid surface and gate (thus, $\mathcal{E}_g$ comes into play twice). Y_{e-} is the mean of an integer-rounded Gaussian with a width of $\sqrt{F_{S2} Y_{e-}}$. F_{S2} is O(1) and captures grid non-uniformity.
- S2.5 A binomial of probability g_1^{gas} (2-D varying) similar to g_1 is step 1 of a process similar to S1.1–4.

More precise S2 simulation is possible in the optional integration of Garfield with NEST, which also possesses an optional G4 integration for simulating E deposits prior to the first step above. More details on the lists here can be found in Section 2.2 of Szydagis et al. (2021a). Section 2.2.4 explains NEST's last layer. All values for the first list are provided in Supplementary Table S4 (Supplementary Appendix SB), and examples for S1 and S2 are provided by Rischbieter (2022), especially in Figure 4.3 left.

2.3 Nuclear recoils (neutrons and WIMPs and Boron-8)

NR N_q' (differentiated in this section from ER with a prime) is well-fit by a power law across >3 orders of magnitude in E [Figure 5 in Szydagis et al. (2021a)]. This is a simplification of the Lindhard approach to modeling the reduced quanta compared with ER but also allows for departures from Lindhard at higher Es, lowering $N_q'(E)$'s rate of change with respect to Lindhard. Fewer equations and parameters are involved compared to Lindhard, which is a combination of multiple power laws inside a rational function (Lindhard, 1963); see Equation 8 in Szydagis et al. (2021a) for more justification. NEST uses that simpler formula:

$$N_q' = aE^b, \text{ where } a = 11^{+2.0}_{-0.5} \text{ and } b = 1.1 \pm 0.05. \tag{9}$$

The uncertainties here are >10 × those reported recently for the same fit as only statistical error was included in Equation 6 of Szydagis et al. (2021a). In this study, systematic uncertainties in S1 detection efficiency and S2 gain (including e^- extraction efficiency) are included. They can be found inside the individual references in the caption of Figure 3. Individual power laws were found for each dataset prior to the error-weighted combination so that a dataset with more points was not overly weighted. Equation 9 was also cross-checked with L_y' and Q_y' individually extracted from data, as displayed in Figure 3, and the raw S1 and S2 data on continuous energy spectrum sources.

Equation 9 can be used to define "quenching," $\mathcal{L}$, in Equation 10:

$$\mathcal{L}(E,\rho) = N_q'(E)\big/N_q(E,\rho) = N_q'(E)\,W_q(\rho)\big/E, \tag{10}$$

which is interpreted as the fraction of total NR energy shared with the electron cloud to produce ions and excitons. $\mathcal{L}$ permits one to define the electron equivalent energy in units of keV$_{ee}$ for NR as $\mathcal{L}$ × (E in keV$_{nr}$), a best average reconstruction of the (combined-)E of recoiling nuclei. This $\mathcal{L}$ should be applicable to neutron calibrations, WIMPs, and CEνNS, such as from ^{8}B nuclear fusion (Aprile et al., 2021).

While the previous equation sets the total quanta, the next equation determines the field- and density-dependent division into individual yields (charge or light) in an anti-correlated fashion, reducing r with higher field:

$$\varsigma(\mathcal{E},\rho) = \gamma\mathcal{E}^{\delta}\left(\frac{\rho}{\rho_0}\right)^{\upsilon}, \text{ where } \gamma = 0.0480 \pm 0.0021 \text{ and}$$
$$\delta = -0.0533 \pm 0.0068, \text{ and } \upsilon = 0.3. \tag{11}$$

The reference density is $\rho_0 \equiv 2.90$ g/cm^3. The value of 2.89 was a specific example using LUX; the differences in yields are negligible. The exponent υ for the density dependence is hypothetical. It is not well-measured at densities significantly deviating from ρ_0 (Dahl, 2009).

We use Equation 11 to produce a Q'_y equation:

$$Q'_y(E,\mathcal{E},\rho) = N_{e^-} \text{ per keV} = \frac{1}{\varsigma(\mathcal{E},\rho)(E+\epsilon)^p}\left(1 - \frac{1}{1+\left(\frac{E}{\zeta}\right)^{\eta}}\right), \text{where}$$
$$\epsilon = 12.6^{+3.4}_{-2.9}\,\text{keV},\ p = 0.5, \zeta = 0.3 \pm 0.1\,\text{keV, and}\, \eta = 2 \pm 1. \tag{12}$$

Energy deposited is again E (in keV), and ϵ is the reshaping parameter for the E dependence. Higher or lower ς decreases or increases the Q'_y level, respectively, providing the field-dependent shape of $Q'_y(E)$. ε can be assumed to be the characteristic E where Q'_y changes in its behavior from ~constant at $O(1\text{ keV})$ to decreasing at $O(10\text{ keV})$ (note that ς has adaptable units of keV^{1-p}).

ζ and η are the two sigmoid parameters that control the Q'_y roll-off at sub-keV energies. They permit a better match to not only the most recent calibrations (Lenardo et al., 2019; Akerib et al., 2017c) but also to NEST versions pre-2.0 and other past models. Combining Thomas–Imel recombination with Lindhard [Equation 8 of Szydagis et al. (2021a)] produces a roll-off in Q'_y, but it is less steep than that observed in data. Here, η controls steepness, allowing for an improved modeling of low-energy NR (Szydagis et al., 2013; Sorensen and Dahl, 2011), while ζ represents a characteristic scale for NR to ionize one e^- (Szydagis et al., 2021a; Sorensen, 2015). At high E, $p = 0.5$ reproduces $Q'_y \propto 1/\sqrt{E}$ (Figure 3, bottom row).

Similar to ER, N_{ph} is derived from $N'_q - N_{e-}$, but this is only a temporary anti-correlation enforcement; an additional sigmoid permits L'_y's flexibility (Equation 13). Future calibration data could show a decrease or even flattening, potentially due to additional N_{ph} from the Migdal effect (Akerib, 2016; Aprile et al., 2019c). An increase in L'_y is possible even as $E \rightarrow 0$. This is not unphysical as long as N_{ph} vanishes in that limit, conserving E.

$$L''_y = \frac{N'_q}{E} - Q'_y.\, N_{ph} = L''_y E\left(1 - \frac{1}{1+\left(\frac{E}{\theta}\right)^{\iota}}\right);\ L'_y = \frac{N_{ph}}{E},$$
$$\text{where}\, \theta = 0.3 \pm 0.05\,\text{keV and}\, \iota = 2 \pm 0.5.\, N'_q = N_{ph} + N_{e^-}. \tag{13}$$

The top row of Figure 3, especially when read from right to left, shows the same L'_y shape at all fields, once again indicative of a zero-field phantom Q'_y. In the L'_y calculation, L''_y is a temporary variable (perfect anti-correlation) used within NEST to calculate the final L'_y and N'_q values. The best-fit numbers for θ and ι match those of their counterparts ζ and η for Q'_y. In this modular but smooth approach, the sigmoidal terms in L'_y and Q'_y approach 1.0 with increasing E. This method allows for separate fitting of the low- and high-E regimes, enabling the possibility of different physics in the sub-keV region, while avoiding the use of higher-E data to over-constrain lower-E yields.

The two sigmoids reduce the predictive power of NEST for extrapolation into newer, lower-E regimes where no calibrations exist. In the case of L'_y, it will be challenging to achieve any with low uncertainty.

θ is a physically motivated characteristic energy for the release of a single (VUV) photon. Like ζ, its value is 300 eV, in agreement with Sorensen (2015) and NEST pre-v2.0.0 (Szydagis et al., 2013). Fundamental physics models for the $\mathcal{L}$ governing total quanta, such as Lindhard (1963) and Hitachi (2005) and Aprile et al. (2006), coupled to the Thomas–Imel "box" model for recombination (Thomas and Imel, 1987), predict a similar value. A larger θ value means more E is needed to produce a single photon (as opposed to excitons), and L'_y is lowered. This may potentially be detectable for an experiment with sufficient light collection efficiency.

Decreasing ι would also lower L'_y, halving L'_y across all E when $\iota = 0$. On the other hand, in the limit of infinite ι (and/or $\theta \rightarrow 0$), the effect of the sigmoid is entirely removed, increasing L'_y at low E. The same is true for η and ζ in the Q'_y formulation. A hard cut-off for any quanta was implemented in NEST for $E < W_q\ (N_q / N'_q) \approx 200$ eV. N_q represents the quanta that would have been generated for same-E ER. Below this, no quanta are generated. Sub-keV recoils have been observed at 200–400 V/cm (Figure 3).

In contrast to ER, for which the data suggest strict anti-correlation, simulated $\langle N'_q \rangle$ is not varied with a common Fano factor shared by both types of quanta for simplicity. For NR, there are (nominally) separate Fano factors for excitation and ionization, which can soften the strict anti-correlation at the level of the fundamental quanta. $\langle N_{ex} \rangle$ is smeared using a Gaussian of standard deviation $\sigma_{ex} = \sqrt{F_{ex}\langle N_{ex} \rangle}$. $\langle N_i \rangle$ is similarly varied using $\sigma_i = \sqrt{F_i \langle N_i \rangle}$, as is the standard practice for Fano factors (Fano, 1947). Based on the sparse existing reports of NR E resolution (Akerib, 2016; Lenardo et al., 2019; Plante, 2012), both F_{ex} and F_i are set to 0.4 in NEST (as of v2.3.11; 1 earlier) although some data imply $F_{ex} \gg 1$ (Akerib, 2016; Plante, 2012). $N_{ex} = G[\langle N_{ex} \rangle, \sigma_{ex}]$ and $N_i = G[\langle N_i \rangle, \sigma_i]$ (G=Gauss).

Using the same functional form as in Equation 8 from ER, NEST models fluctuations in recombination for the redistribution of photons and electrons prior to measurable NR S1 and S2. The new parameters are distinguished using a prime symbol superscript again for NR ($'$).

Parameter values are similar but not identical to those from ER: $A' = 0.04$ (as of v2.3.11 and fixed for all fields), $\xi' = 0.50$, and $\omega' = 0.19$ ($\alpha'_p = 0$). Over time, these appear to have been converging upon values similar to ER's. These set a final recombination width σ'_r. N_{e-} and N_{ph} distributions have that width but are skewed due to NR recombination asymmetry ($\alpha'_r = 2.25$). α'_r may be higher, but it is difficult to disambiguate NR skew (less L_y) in data from unresolved multiple scatters, other detector effects (Akerib et al., 2020b), or Migdal effect ER, which can increase Q_y and generate a secondary population (Akerib et al., 2019b).

3 Comparisons to first-principles approaches

By smoothly interpolating datasets taken at individual energies and/or electric fields, NEST is now fully empirical, built upon sigmoids and power laws as needed for a continuous model.

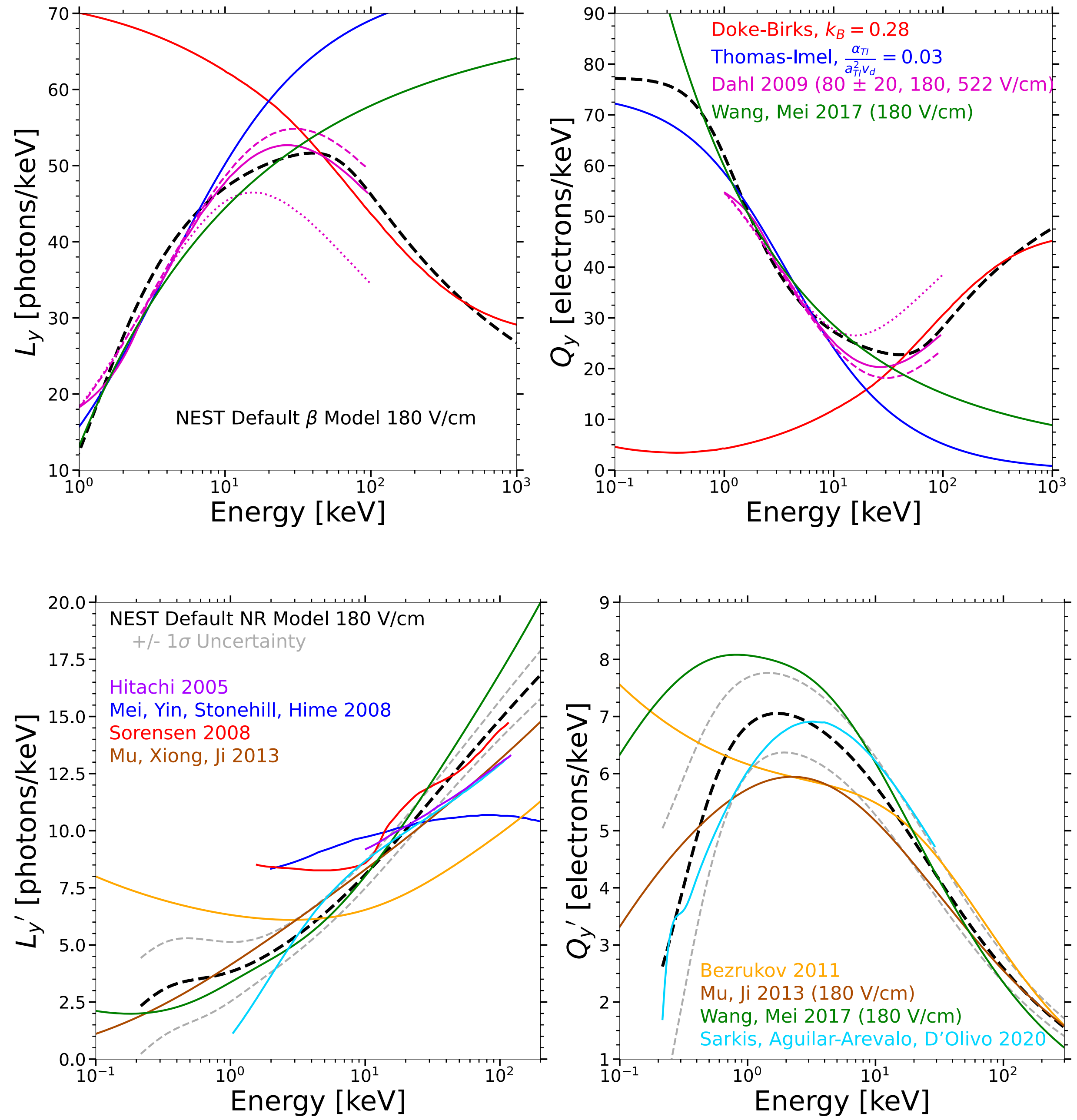

FIGURE 4
Comparing NEST with other approaches: L_y (left) and Q_y (right) alternate, for ER (top) and NR (bottom), at 180 V/cm (Doke et al., 2002; Thomas and Imel, 1987; Dahl, 2009; Wang and Mei, 2017). The right legends apply to both the left and right plots. This was LUX's initial field (Akerib et al., 2014), in between XENON1T at 80 (Aprile et al., 2020b) and earlier works like Aprile et al. (2011) as high as 730 V/cm. Although similar to fundamental approaches, NEST incorporates features of multiple, splitting differences and following the data. The Thomas–Imel (T-I) and Doke/ Birks sample curves shown are meant to match 180 V/cm the most closely. Unlike the T-I and plasma models, NEST accounts for the high-E (low-dE/dx) L_y decrease (Q_y increase) (Wang and Mei, 2017). Birks' law is also applicable but fails to work at low Es (high dE/dx) (Birks, 1964). Dahl presented variations in T-I, utilizable for high Es by breaking up tracks into boxes, although his closest fields were 80 and 522 V/cm (Dahl, 2009). We show a 180-V/cm model (solid), *i.e.*, the weighted average of his 80 (dashed) and 522 V/cm (dotted) models. There are more NR models (right) for explaining potential WIMPs (Wang and Mei, 2017; Hitachi, 2005; Mei et al., 2008; Sorensen et al., 2009; Mu et al., 2015; Bezrukov et al., 2011; Mu and Ji, 2015; Sarkis et al., 2020). Older models based on L_{eff}, which was L_y' relative to ^{57}Co γ-rays (122 keV), were translated assuming 64 photons/keV at 0 V/cm with a small error (Szydagis et al., 2011; Lenardo et al., 2015), unless papers had a different value, which we then used instead (Bezrukov: 53). If they presented multiple models, we plot the most central one and/or one closest to data. Comparisons are only qualitative, ensuring NEST has the correct, physically motivated shape across different regimes.

However, inherent uncertainty is introduced by extrapolating into new energy and/or field regimes. To assess that and further validate an empirical approach, we show agreement with the models closer to "first principles." Within NEST's earliest versions, the Thomas–Imel (T-I) box model (Thomas and Imel, 1987) was used for low energy, while Birks' law of scintillation was adapted for high energy. Both were qualitatively explained in Section 2.1 but are quantified in this section. The latter approach inside NEST was similar to Doke's modification (Szydagis et al., 2011) for scintillation alone but applied directly to recombination, allowing it to model both L_y and Q_y:

$$\langle r\rangle = \frac{k_A \frac{dE}{dx}}{1 + k_B \frac{dE}{dx}} + k_C, \text{ with } k_C = 1 - k_A/k_B. \tag{14}$$

This is Birks' law for other scintillators (Birks, 1964) but with an additional constant k_C that accounts for parent-ion recombination (Doke et al., 2002). Its constraint ensures that $\langle r\rangle$ is between 0 and 1 as it is a probability. A best fit to ER (γ) data has a non-zero k_C only at 0 V/cm; at non-zero $\mathcal{E}$, Equation 14 contains only one Birks' constant, $k_A = k_B$.

k_B's best-fit value (for 180 V/cm) is 0.28 from a fit to only the high-E portion of the NEST β ER model. That model is, in turn, supported by ^{3}H, ^{14}C, and ^{220}Rn data from LUX and XENON. Notably, k_B in NEST v0.9x and the first NEST paper, 13 years ago, for this $\mathcal{E}$ was 0.257, within 10% of the value in Figure 4 (upper right plot pane), which covers many alternative approaches to NEST.

Despite Birks' great success in explaining data at high E, that model cannot capture the behavior of ER at $E \lesssim$ 50 keV. Although lower-E extensions are possible, such as the addition of higher-order terms in dE/dx for that region, we instead consider the T-I model for lower E:

$$\langle r\rangle = 1 - \frac{\ln(1+\xi_{TI})}{\xi_{TI}}, \text{ where } \xi_{TI} = \frac{N_i}{4}\frac{\alpha_{TI}}{a_{TI}^2 v_d}. \tag{15}$$

ξ_{TI} parameterizes the physical principles. α_{TI} describes diffusion, v_d is the e^- drift velocity, and N_i is again the number of ions. Diffusion is modeled using the relation $\alpha_{TI} = De^2/(kT\epsilon_d)$, where D combines e^- and positive-ion diffusion coefficients, e is the elementary charge, k is the Boltzmann constant not Birks, T is temperature, and $\epsilon_d = 1.85 \times \epsilon_0$ is the dielectric constant. $D = 18.3$ cm^2/s is the longitudinal diffusion constant for e^-s at 180 V/cm, derived from S2 pulse lengths (Sorensen, 2011b). e^- diffusion dominates over cation diffusion. Assuming this D (and $T = 173$ K from earlier), ϵ_d as defined above, and taking $v_d = 1.51$ mm/μs at field $\mathcal{E} = 180$ V/cm (Akerib et al., 2016b), we find $\alpha_{TI} = 1.20 \times 10^{-9}$ m^3/s. From this, the escape probability $(1 - \langle r\rangle)$ for electrons inside a box is found by solving the relevant (Jaffé) differential equations (refer to Section 6.2 of Dahl (2009) for the details).

We interpret a_{TI}, the size of the "box" surrounding ionized atoms, as corresponding to an ($\mathcal{E}$-independent) e^--ion thermalization distance of 4.6 μm, as calculated by Mozumder (1995). This value was used before as a border in NEST for track length to switch from T-I to Birks. The ultimate value of TIB $\equiv \alpha_{TI}/(a_{TI}^2 v_d)$ for that case is 0.0376.

Dahl found best-fit values of TIB ranging from 0.03 to 0.04 for both ER and NR data at 60–522 V/cm (Dahl, 2009). Our contemporary fits (for NEST and data), the blue lines at low energies in the first two panels at top in Figure 4, used 0.0300. If v_d changes with the drift field [it is typically O(2 mm/μs) (Albert et al., 2017)], then the entire ranges described by Dahl, and by Sorensen and Dahl, are covered: 0.02–0.05 (Sorensen and Dahl, 2011).

For NR, Figure 4 (bottom row) presents many different past models, mainly for L_y. NEST originally used T-I for NR, as described by Dahl (2009) and Sorensen and Dahl (2011), represented by the blue lines in Figure 5. This follows the same color convention as Figure 4. T-I fixes r, thus partitioning E into L_y and Q_y; however, the total yield must still be determined. For maximal distinction, we have selected the original Lindhard formula, as laid out by Lindhard (1963); Sorensen and Dahl (2011); Akerib (2016); and Szydagis et al. (2021a), rather than Equation 9. We set the crucial Lindhard parameter of k_L to a value of 0.166, the decades-old default for Xe (Lindhard, 1963). Averaging over E, $N_q'/N_q \approx k_L$. It is observed that 0.166 is consistent with actual data (Akerib, 2016), Lenardo's meta-analysis (Lenardo et al., 2015), and NEST v2.3+.

We identify ς from Equation 12 with the TIB value, as justified by Equation 11, where the parameters for the $\mathcal{E}$ dependence of ς (γ and δ) overlap at the 1σ level with the power-law field dependence of TIB from Lenardo et al. (2015). At 180 V/cm, $\varsigma = 0.0362$, which is quite close to earlier theoretical calculation and comparable to a best-fit TIB for ER, assuming $N_{ex}/N_i = 1.0$. Although higher than for ER, it is the most common assumption for NR, and best-fit values from data and theory vary from 0.7 to 1.1 (Sorensen and Dahl, 2011).

An additional quenching is applied to just L_y' (Manzur et al., 2010). We find a common parameterization of this effect (Bezrukov et al., 2011) to be defined in a manner analogous to Birks' law or Equation 14:

$$q = \frac{1}{1 + \kappa\epsilon_Z^{\lambda}}, \text{ with } \epsilon_Z \approx 10^{-3}E, \tag{16}$$

where $q < 1$ is a multiplicative factor on L_y'. ϵ_Z is unitless reduced energy, useful for comparison between elements. Equation 16 is similar to Equation 14. The power law can be identified as proportional to NR dE/dx. If we define dE/dx (or LET) as approximately $\beta'\epsilon^{\lambda}$, then $\kappa = k_B\beta'\mathcal{L}$. Assuming ER k_B (defined as 0.28 for 180 V/cm in Figure 4 top), $\mathcal{L} \sim 0.15$ (11/73) per an energy-independent approximation of Equation 9, justified by the power being close to 1, and with $\beta' = 100$, we obtain $\kappa = 4.20$, $< 0.2\sigma$ away from that determined by Lenardo et al. (2015). A fraction of the quanta removed from L_y' in Equation 16 may be convertible into Q_y'. Figure 5 (right) explores that with the fraction set to 0.1.

Unlike with ER, Birks' law models NR over the entire E range of interest (Figure 5, red), with $k_B = 0.28$ and $dE/dx = \beta'\epsilon^{\lambda} = 100\epsilon$. Although there is disagreement about whether λ is 1.0 or 0.5 depending on the E regime (Hitachi, 2005; Aprile et al., 2006), 1.0 only differs by 1.6σ from the value of 1.14, as determined by Lenardo et al. (2015).

Looking back at alternatives to Lindhard, Figure 4 shows that NEST's power law models for L_y' and Q_y' align well with results from Mu et al. (2015) and Mu and Ji (2015), and Wang and Mei (2017) and Mei et al. (2008). NEST's lower 1σ line intersects with L_y' determined by Sarkis et al. (2020), which is low due to the exclusion of more recent data points (Akerib, 2016; Akerib, 2022). On the higher-E L_y' end, NEST's upper uncertainty band encompasses results from neriX (Aprile et al., 2018b). For Q_y', NEST lies in between higher values of Wang and Mei (2017) and lower values of Mu and Ji (2015) and Sarkis et al. (2020), also fitting between data from LUX D–D (Akerib, 2016) and LLNL (Lenardo et al., 2019).

The good agreement between the fully empirical NEST model and the first-principle models of both NR and ER shown in this study demonstrates that NEST can accurately simulate potential dark matter signals and backgrounds, respectively. This should hold true even for the regimes where data are still lacking, or they exist but have large uncertainties. In the case of NR, the fully empirical

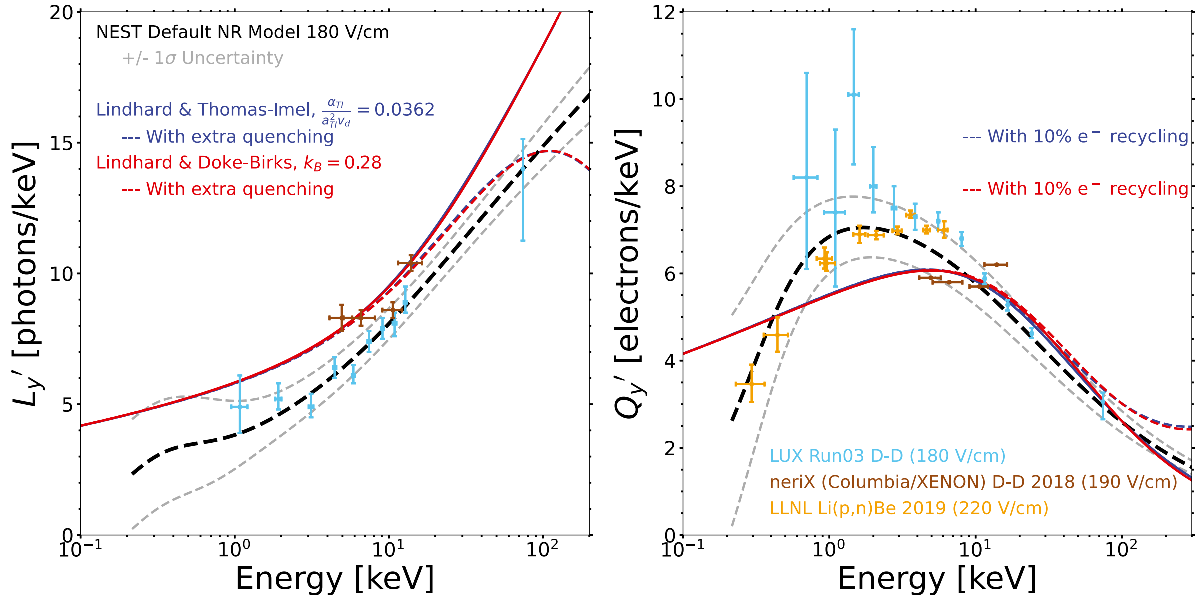

FIGURE 5
Comparisons of NEST and selected NR data to only the Thomas−Imel box (blue) and Birks (red) models of recombination, always using Lindhard to define N_q' (found as Equation 8 in Szydagis et al. (2021a) and elsewhere). For L_y', the dashed lines indicate additional quenching at higher Es and dE/dx, while for Q_y', where this quenching has no direct impact, the dotted lines indicate the partial conversion of photons into e⁻s from that effect (or not, solid lines). Some datasets, including at other fields, are consistent at a 1−2σ level with no quenching or conversion, not the amounts shown. The L_y' data from 50 to 100 keV$_{nr}$ are inconsistent: see Figure 3 (upper left) and Plante et al. (2011).

approach reproduces all data more accurately while using a comparable number of free parameters, offering much greater flexibility than semi-empirical approaches. For fluctuations, the number of NEST free parameters increased to two Fano factors (excitation and ionization) and four numbers for recombination width and skew to fully model the E resolution. NEST, justified first using data, is not limited to the operating conditions of previous experiments to make predictions relevant for a future experiment, although L_y and Q_y must pass through a detector simulation to obtain realistic S1 and S2 pulse areas: the processes in Section 2.2.5 in this study and Supplementary Appendix SA of James et al. (2022).

4 Discussion and future work

Beginning with our models of beta ER, gamma-ray ER, and the NR light and charge yields, along with resolution modeling, a coherent picture was built up inside the NEST framework, which enables a good agreement with data. NEST was also shown to have features from multiple first-principles approaches, such as the box and Birks models. NEST already works for LAr (Szydagis et al., 2021a) using the same formulas as LXe but with unique parameter values. However, it still only works best for point-like interactions, like those in dark matter experiments like DarkSide, not tracks, as will be observed by DUNE. The list of NEST collaborators includes TESSERACT (Biekert et al., 2022) members, so the addition of liquid helium (LHe) to NEST is planned.

Looking beyond LHe, short-term future work includes NEST re-writing to account for the lower W_q measured by EXO and Anton et al. (2020); Baudis et al. (2021), but this will be easier if NEST can return to approaches closer to first principles. Therefore, a concerted effort will be made to revisit a semi-empirical formulation through the application of a modified T-I model, as pioneered by ArgoNeuT (Acciarri et al., 2013); this approach will incorporate a literal breakup of long tracks into boxes, as described in the thesis of Dahl, allowing higher energies to exhibit lower light yields without hard-coding this behavior, by virtue of being composed of multiple lower-E interaction sites. High-E modeling is thus accomplished by having one model for all Es but treating high-E interactions as a series of many low-E fragments, where L_y will continue to be monotonically increasing with E. The main motivation for this is greater confidence in extrapolations to uncalibrated regions of future detectors.

The modified box model of LArTPC-based high-E neutrino experiments should also be useful for LXe NR. We demonstrate, herein, how it represents a more generalized version of the current NR model:

$$Q_y' = \frac{N_{e-}}{E} = (1-r)\frac{N_i}{E} = \frac{\ln(a'+\xi)}{\xi}\frac{N_i}{E} = \frac{\ln(a'+\xi)}{\xi}\frac{N_q/E}{1+\alpha_x} = \frac{\ln(a'+\xi)}{\xi E}\frac{aE^b}{1+\alpha_x}, \tag{17}$$

where $a' \equiv 1$ in default T-I [but relaxing this constraint to $O(1)$ as per Acciarri et al. (2013) can better fit data], ξ is short for ξ_{TI}, redefined as $\beta\, dE/dx$ with β as a constant (not Equation 15), and $\alpha_x \equiv N_{ex}/N_i$ for conciseness.

$$Q_y' = \frac{aE^{b-1}}{1+\alpha_x}\frac{\ln\left(1+\beta\frac{dE}{dx}\right)}{\beta\frac{dE}{dx}} \approx \frac{a}{1+\alpha_x}\frac{\ln\left(1+\beta\frac{dE}{dx}\right)}{\beta\frac{dE}{dx}}$$

$$\approx \frac{a}{2}\frac{\ln\left(1+\beta\frac{dE}{dx}\right)}{\beta\frac{dE}{dx}} \approx 5\frac{\ln\left(1+\beta\frac{dE}{dx}\right)}{\beta\frac{dE}{dx}}, \tag{18}$$

where we employ, in order, the approximations $b \approx 1$, $\alpha_x \approx 1$, and $a \approx 10$ (Equation 9). Fitting to the SRIM line in Figure 5 of Aprile et al. (2006), one finds that for NR, in normalized (dimensionless) units, stopping power is

$$dE\big/dx = 120\sqrt{\epsilon_Z} = 120\sqrt{0.001E} = 120\sqrt{0.001}\sqrt{E} = 3.8\sqrt{E}, \quad (19)$$

which is valid in the range of 0–100 keV. However, near 50 keV, a square root function with an offset also fits SRIM: $3.4\sqrt{E+\epsilon}$, with $\epsilon = 12.6$ keV (Equation 12). Making the ansatz $\beta \sim \varsigma$ (Equation 11),

$$Q_y' \approx 5\frac{\ln\left(1+\varsigma\frac{dE}{dx}\right)}{\varsigma\frac{dE}{dx}} = 5\frac{\ln\left(1+0.036\,3.4\,\sqrt{E+12.6}\,\right)}{0.036\,3.4\,\sqrt{E+12.6}} = \frac{5}{3.4}\,\frac{0.677}{\varsigma\sqrt{E+\epsilon}}$$
$$= \frac{1}{\varsigma\sqrt{E+\epsilon}}, \quad (20)$$

recovering the high-E portion of Equation 12 at $\varsigma = 0.036$ (200 V/cm) and $E = 50$ keV, given Equations 18–20. By modifying the power law for N_q to be $aE^b - C$ (McMonigle, 2024), it may be possible to eliminate the need for the sigmoids for reducing both Q_y and L_y at the lowest Es, combining C with an additional degree of freedom, a non-unity a' in the natural log. By replacing our present Equations 12, 20 with Equation 17, we should be able to find a sufficiently flexible compromise that fits data with the same number of free parameters or fewer even (eliminating the sigmoid roll-offs and the ϵ offset in dE/dx potentially), all motivated from first principles (T-I). The redefinition of ξ_{TI} in terms of dE/dx permits a non-linearity in the dependence of ξ on N_i and an incorporation of dE/dx (as in the Doke/ Birks' law), while α_x could be made E and $\mathcal{E}$-dependent as in **Eq. B8** of Aprile (2024b), if absolutely necessary, following the similar increase with E for ER in Equation 2 [mimicked by **Eq. A4**'s exponential in Aprile (2024b)]. Lastly, the replacement of $aE^b - C$ with E/W_q in Equation 17 could permit usage for ER, as in LAr, from the keV to the GeV scales.

Improved modeling of the MeV (ERs) scale is important for searches for neutrinoless double-beta ($0\nu\beta\beta$) decay, for which the key discrimination is not NR vs. ER but between two forms of the latter (β vs. γ). EXO-200 (Anton et al., 2019) and KamLAND-Zen (Abe et al., 2023) have produced the two most stringent half-life limits for ^{136}Xe and are highly competitive with the Ge-based experiments. In addition to these results, one must evaluate the prospects of nEXO (Albert et al., 2018), LZ (Akerib et al., 2020c), XENONnT (Aprile et al., 2022), and XLZD (Aalbers et al., 2022) for this field of nuclear physics. Dark-matter-focused experiments have greater ER backgrounds than nEXO but superior energy resolution.

Long-term future work on NEST will involve an *ab initio* MC approach incorporating cross sections for recombination and the other relevant processes (Piazza et al., 2025), and molecular dynamics modeling of Xe atoms with the 12-6 Lennard-Jones potential for van der Waals forces will be explored (Equation 21). The LXe values for the L-J parameters as well as for other, more advanced versions of the model are well-established (Rutkai et al., 2017):

$$V(d) = 4\epsilon_{LJ}\left[\left(\frac{R}{d}\right)^{12} - \left(\frac{R}{d}\right)^{6}\right], \text{ where } \epsilon_{LJ} = 1.77\,\text{kJ/mol and}$$
$$R = 4.10\ \text{Å}. \quad (21)$$

While these approaches are challenging at high (MeV) energies, they become more feasible at sub-keV scales, where yields are more uncertain; *e.g.*, for ^{8}B, fewer interactions are involved, leading to a more computationally tractable problem.

Data availability statement

The datasets presented in this study can be found in online repositories. The names of the repository/repositories and accession number(s) can be found at: https://github.com/NESTCollaboration/nest.

Author contributions

MS: conceptualization, data curation, formal analysis, funding acquisition, investigation, methodology, project administration, resources, software, supervision, validation, visualization, writing–original draft, and writing–review and editing. JB: formal analysis, software, and writing–review and editing. GB: formal analysis, software, and writing–review and editing. JB: software and writing–review and editing. EB: investigation, supervision, validation, and writing–review and editing. JC: formal analysis, software, visualization, and writing–review and editing. SF: formal analysis, software, visualization, and writing–original draft. JH: formal analysis, software, and writing–review and editing. AK: resources, software, supervision, and writing–review and editing. EK: formal analysis, investigation, software, validation, visualization, writing–original draft, and writing–review and editing. CL: formal analysis, software, and writing–original draft. DM: investigation, resources, software, supervision, validation, and writing–review and editing. KM: formal analysis, software, and writing–review and editing. RM: software, validation, and writing–review and editing. MM: methodology, resources, software, supervision, validation, and writing–review and editing. JM: formal analysis, software, and writing–review and editing. KN: conceptualization, funding acquisition, investigation, methodology, resources, software, supervision, writing–original draft, and writing–review and editing. GR: conceptualization, data curation, formal analysis, investigation, methodology, project administration, resources, software, supervision, validation, visualization, writing–original draft, and writing–review and editing. KT: formal analysis, software, and writing–review and editing. MT: conceptualization, data curation, funding acquisition, investigation, methodology, project administration, resources, software, supervision, validation, and writing–original draft. CT: conceptualization, data curation, funding acquisition, investigation, methodology, project administration, resources, software, supervision, writing–original draft, and writing–review and editing. VV: conceptualization, data curation, formal analysis, investigation, methodology, project administration, software, supervision, validation, visualization, writing–original draft, and writing–review and editing. SW: supervision, validation, and writing–review and editing. MW: formal analysis and writing–review and editing. ZZ: formal analysis, software, and writing–review and editing. MZ: data curation, formal analysis, investigation, software, validation, visualization, writing–original draft, and writing–review and editing.

Funding

The author(s) declare that financial support was received for the research, authorship, and/or publication of this article. This work was supported by the U.S. Department of Energy (DOE) under Awards DE-SC0015535, DE-SC0024225, DE-SC0021388, DE-SC0018982 and DE-AC02-05CH11231, and by the National Science Foundation (NSF) under Awards 2046549 and 2112802.

Acknowledgments

The authors thank the LZ/LUX plus XENON1T/nT/DARWIN collaborations for useful recent discussion and continued support for NEST work. They especially thank LUX for providing key detector parameters and LUX collaborator Prof. Rick Gaitskell (of Brown University), Xin Xiang (formerly of Brown, now at Brookhaven National Laboratory), and Quentin Riffard (Lawrence Berkeley National Laboratory) for critical discussions regarding the detector performance of a potential Generation-3 liquid Xe TPC detector.

Conflict of interest

Author JC was employed by company Deepgram.

The remaining authors declare that the research was conducted in the absence of any commercial or financial relationships that could be construed as a potential conflict of interest.

Publisher's note

Supplementary material

The Supplementary Material for this article can be found online at: https://www.frontiersin.org/articles/10.3389/fdest.2024.1480975/full#supplementary-material

References

Aalbers, J., AbdusSalam, S. S., Abe, K., Aerne, V., Agostini, F., Ahmed Maouloud, S., et al. (2022). A next-generation liquid xenon observatory for dark matter and neutrino physics. *J. Phys. G Nucl. Part. Phys.* 50, 013001. doi:10.1088/1361-6471/ac841a

Aalbers, J., Akerib, D., Akerlof, C., Al Musalhi, A., Alder, F., Alqahtani, A., et al. (2023). First dark matter search results from the LUX-ZEPLIN (LZ) experiment. *Phys. Rev. Lett.* 131, 041002. doi:10.1103/physrevlett.131.041002

Aalbers, J., Akerib, D., Al Musalhi, A., Alder, F., Amarasinghe, C., Ames, A., et al. (2024). First constraints on WIMP-nucleon effective field theory couplings in an extended energy region from LUX-ZEPLIN. *Phys. Rev. D.* 109, 092003. doi:10.1103/physrevd.109.092003

Abe, S., Asami, S., Eizuka, M., Futagi, S., Gando, A., Gando, Y., et al. (2023). Search for the majorana nature of neutrinos in the inverted mass ordering region with KamLAND-zen. *Phys. Rev. Lett.* 130, 051801. doi:10.1103/PhysRevLett.130.051801

Abud, A. A., Abi, B., Acciarri, R., Acero, M., Adames, M., Adamov, G., et al. (2023). Identification and reconstruction of low-energy electrons in the ProtoDUNE-SP detector. *Phys. Rev. D.* 107, 092012. doi:10.1103/PhysRevD.107.092012

Acciarri, R., Adams, C., Asaadi, J., Baller, B., Bolton, T., Bromberg, C., et al. (2013). A study of electron recombination using highly ionizing particles in the ArgoNeuT Liquid Argon TPC. *JINST* 8, P08005. doi:10.1088/1748-0221/8/08/p08005

Akerib, D., Alsum, S., Araújo, H., Bai, X., Balajthy, J., Baxter, A., et al. (2019a). Improved measurements of the β-decay response of liquid xenon with the LUX detector. *Phys. Rev. D.* 100 022002. doi:10.1103/PhysRevD.100.022002

Akerib, D. S. (2016). Low-energy (0.7-74 keV) nuclear recoil calibration of the LUX dark matter experiment using D-D neutron scattering kinematics. *arXiv:1608.05381*. doi:10.48550/arXiv.1608.05381

Akerib, D. S. (2022). Improved dark matter search sensitivity resulting from LUX low-energy nuclear recoil calibration. *arXiv:2210.05859*. doi:10.48550/ARXIV.2210.05859

Akerib, D. S., Akerlof, C., Alqahtani, A., Alsum, S., Anderson, T., Angelides, N., et al. (2021b). Simulations of events for the LUX-ZEPLIN (LZ) dark matter experiment. *Astropart. Phys.* 125, 102480. doi:10.1016/j.astropartphys.2020.102480

Akerib, D. S., Akerlof, C. W., Alqahtani, A., Alsum, S. K., Anderson, T. J., Angelides, N., et al. (2020c). Projected sensitivity of the LUX-ZEPLIN experiment to the 0νββ decay of ^{136}Xe. *Phys. Rev. C* 102 014602. doi:10.1103/PhysRevC.102.014602

Akerib, D. S., Alsum, S., Araújo, H., Bai, X., Bailey, A., Balajthy, J., et al. (2017c). Results from a search for dark matter in the complete LUX exposure. *Phys. Rev. Lett.* 118, 021303. doi:10.1103/PhysRevLett.118.021303

Akerib, D. S., Alsum, S., Araújo, H., Bai, X., Bailey, A., Balajthy, J., et al. (2017b). Signal yields, energy resolution, and recombination fluctuations in liquid xenon. *Phys. Rev. D.* 95, 012008. doi:10.1103/PhysRevD.95.012008

Akerib, D. S., Alsum, S., Araújo, H., Bai, X., Bailey, A., Balajthy, J., et al. (2017a). Ultra-low energy calibration of LUX detector using ^{127}Xe electron capture. *Phys. Rev. D.* 96, 112011. doi:10.1103/PhysRevD.96.112011

Akerib, D. S., Alsum, S., Araújo, H., Bai, X., Balajthy, J., Baxter, A., et al. (2021a). Effective field theory analysis of the first LUX dark matter search. *Phys. Rev. D.* 103, 122005. doi:10.1103/PhysRevD.103.122005

Akerib, D. S., Alsum, S., Araújo, H., Bai, X., Balajthy, J., Baxter, A., et al. (2020a). Improved modeling of β electronic recoils in liquid xenon using LUX calibration data. *J. Instrum.* 15, T02007. doi:10.1088/1748-0221/15/02/t02007

Akerib, D. S., Alsum, S., Araújo, H., Bai, X., Balajthy, J., Baxter, A., et al. (2020b). Discrimination of electronic recoils from nuclear recoils in two-phase xenon time projection chambers. *Phys. Rev. D.* 102, 112002. doi:10.1103/PhysRevD.102.112002

Akerib, D. S., Alsum, S., Araújo, H., Bai, X., Balajthy, J., Beltrame, P., et al. (2019b). Results of a search for sub-GeV dark matter using 2013 LUX data. *Phys. Rev. Lett.* 122, 131301. doi:10.1103/PhysRevLett.122.131301

Akerib, D. S., Araújo, H., Bai, X., Bailey, A., Balajthy, J., Bedikian, S., et al. (2014). First results from the LUX dark matter experiment at the Sanford Underground Research Facility. *Phys. Rev. Lett.* 112, 091303. doi:10.1103/PhysRevLett.112.091303

Akerib, D. S., Araújo, H., Bai, X., Bailey, A., Balajthy, J., Beltrame, P., et al. (2016b). Improved limits on scattering of weakly interacting massive particles from reanalysis of 2013 LUX data. *Phys. Rev. Lett.* 116, 161301. doi:10.1103/PhysRevLett.116.161301

Akerib, D. S., Araújo, H., Bai, X., Bailey, A., Balajthy, J., Beltrame, P., et al. (2016a). Tritium calibration of the LUX dark matter experiment. *Phys. Rev. D.* 93, 072009. doi:10.1103/physrevd.93.072009

Akimov, D., Afanasyev, V., Alexandrov, I., Belov, V., Bolozdynya, A., Burenkov, A., et al. (2014). Experimental study of ionization yield of liquid xenon for electron recoils in the energy range 2.8–80 keV. *JINST* 9, P11014. doi:10.1088/1748-0221/9/11/p11014

Akimov, D., Bewick, A., Davidge, D., Dawson, J., Howard, A., Ivaniouchenkov, I., et al. (2002). Measurements of scintillation efficiency and pulse shape for low energy recoils in liquid xenon. *Phys. Lett. B* 524, 245–251. doi:10.1016/s0370-2693(01)01411-3

Albert, J., Barbeau, P. S., Beck, D., Belov, V., Breidenbach, M., Brunner, T., et al. (2017). Measurement of the drift velocity and transverse diffusion of electrons in liquid xenon with the EXO-200 detector. *Phys. Rev. C* 95, 025502. doi:10.1103/PhysRevC.95.025502

Albert, J. B., Anton, G., Arnquist, I. J., Badhrees, I., Barbeau, P., Beck, D., et al. (2018). Sensitivity and discovery potential of the proposed nEXO experiment to neutrinoless double-β decay. *Phys. Rev. C* 97 065503. doi:10.1103/PhysRevC.97.065503

Alvarez, V., Borges, F., Cárcel, S., Castel, J., Cebrián, S., Cervera, A., et al. (2013). Near-intrinsic energy resolution for 30–662 keV gamma rays in a high pressure xenon electroluminescent TPC. *Nucl. Instrum. Methods Phys. Res. Sect. A Accel. Spectrom. Detect. Assoc. Equip.* 708, 101–114. doi:10.1016/j.nima.2012.12.123

Amoruso, S., Antonello, M., Aprili, P., Arneodo, F., Badertscher, A., Baiboussinov, B., et al. (2004). Study of electron recombination in liquid argon with the ICARUS TPC. *Nucl. Instrum. Methods Phys. Res. Sect. A Accel. Spectrom. Detect. Assoc. Equip.* 523, 275–286. doi:10.1016/j.nima.2003.11.423

Anton, G., Badhrees, I., Barbeau, P., Beck, D., Belov, V., Bhatta, T., et al. (2019). Search for neutrinoless double-β decay with the complete EXO-200 dataset. *Phys. Rev. Lett.* 123 161802. doi:10.1103/PhysRevLett.123.161802

Anton, G., Badhrees, I., Barbeau, P. S., Beck, D., Belov, V., Bhatta, T., et al. (2020). Measurement of the scintillation and ionization response of liquid xenon at MeV energies in the EXO-200 experiment. *Phys. Rev. C* 101, 065501. doi:10.1103/PhysRevC.101.065501

Aprile, E. (2024a). First measurement of solar ^{8}B neutrinos via coherent elastic neutrino-nucleus scattering with XENONnT. *arXiv:2408.02877.*

Aprile, E. (2024b). XENONnT WIMP search: signal & background modeling and statistical inference.

Aprile, E., Aalbers, J., Agostini, F., Ahmed Maouloud, S., Alfonsi, M., Althueser, L., et al. (2021). Search for coherent elastic scattering of solar ^{8}B neutrinos in the XENON1T dark matter experiment. *Phys. Rev. Lett.* 126, 091301. doi:10.1103/PhysRevLett.126.091301

Aprile, E., Aalbers, J., Agostini, F., Alfonsi, M., Althueser, L., Amaro, F., et al. (2020b). Excess electronic recoil events in XENON1T. *Phys. Rev. D.* 102, 072004. doi:10.1103/PhysRevD.102.072004

Aprile, E., Aalbers, J., Agostini, F., Alfonsi, M., Althueser, L., Amaro, F., et al. (2019c). Search for light dark matter interactions enhanced by the Migdal effect or bremsstrahlung in XENON1T. *Phys. Rev. Lett.* 123, 241803. doi:10.1103/physrevlett.123.241803

Aprile, E., Aalbers, J., Agostini, F., Alfonsi, M., Althueser, L., Amaro, F., et al. (2019b). XENON1T dark matter data analysis: signal and background models and statistical inference. *Phys. Rev. D.* 99, 112009. doi:10.1103/PhysRevD.99.112009

Aprile, E., Aalbers, J., Agostini, F., Alfonsi, M., Althueser, L., Amaro, F. D., et al. (2019a). Observation of two-neutrino double electron capture in ^{124}Xe with XENON1T. *Nature* 568, 532–535. doi:10.1038/s41586-019-1124-4

Aprile, E., Aalbers, J., Agostini, F., Alfonsi, M., Althueser, L., Amaro, F. D., et al. (2020a). Energy resolution and linearity of XENON1T in the MeV energy range. *Eur. Phys. J. C* 80, 785. doi:10.1140/epjc/s10052-020-8284-0

Aprile, E., Aalbers, J., Agostini, F., Alfonsi, M., Amaro, F., Anthony, M., et al. (2017). First dark matter search results from the XENON1T experiment. *Phys. Rev. Lett.* 119, 181301. doi:10.1103/PhysRevLett.119.181301

Aprile, E., Aalbers, J., Agostini, F., Alfonsi, M., Amaro, F., Anthony, M., et al. (2018a). Signal yields of keV electronic recoils and their discrimination from nuclear recoils in liquid xenon. *Phys. Rev. D.* 97, 092007. doi:10.1103/PhysRevD.97.092007

Aprile, E., Abe, K., Agostini, F., Ahmed Maouloud, S., Alfonsi, M., Althueser, L., et al. (2022). Double-weak decays of ^{124}Xe and ^{136}Xe in the XENON1T and XENONnT experiments. *Phys. Rev. C* 106, 024328. doi:10.1103/PhysRevC.106.024328

Aprile, E., Angle, J., Arneodo, F., Baudis, L., Bernstein, A., Bolozdynya, A., et al. (2011). Design and performance of the XENON10 dark matter experiment. *Astropart. Phys.* 34, 679–698. doi:10.1016/j.astropartphys.2011.01.006

Aprile, E., Anthony, M., Lin, Q., Greene, Z., de Perio, P., Gao, F., et al. (2018b). Simultaneous measurement of the light and charge response of liquid xenon to low-energy nuclear recoils at multiple electric fields. *Phys. Rev. D.* 98, 112003. doi:10.1103/PhysRevD.98.112003

Aprile, E., Arisaka, K., Arneodo, F., Askin, A., Baudis, L., Behrens, A., et al. (2010). First dark matter results from the XENON100 experiment. *Phys. Rev. Lett.* 105, 131302. doi:10.1103/PhysRevLett.105.131302

Aprile, E., Baudis, L., Choi, B., Giboni, K. L., Lim, K., Manalaysay, A., et al. (2009). New measurement of the relative scintillation efficiency of xenon nuclear recoils below 10 keV. *Phys. Rev. C* 79, 045807. doi:10.1103/PhysRevC.79.045807

Aprile, E., Bolotnikov, A. E., Bolozdynya, A. L., and Doke, T. (2008). *Noble gas detectors*. Wiley. doi:10.1002/9783527610020

Aprile, E., Budnik, R., Choi, B., Contreras, H. A., Giboni, K. L., Goetzke, L. W., et al. (2012). Measurement of the scintillation yield of low-energy electrons in liquid xenon. *Phys. Rev. D.* 86, 112004. doi:10.1103/PhysRevD.86.112004

Aprile, E., Dahl, C. E., de Viveiros, L., Gaitskell, R. J., Giboni, K. L., Kwong, J., et al. (2006). Simultaneous measurement of ionization and scintillation from nuclear recoils in liquid xenon for a dark matter experiment. *Phys. Rev. Lett.* 97, 081302. doi:10.1103/PhysRevLett.97.081302

Aprile, E., Giboni, K. , Majewski, P., Ni, K., Yamashita, M., Hasty, R., et al. (2005). Scintillation response of liquid xenon to low energy nuclear recoils. *Phys. Rev. D.* 72, 072006. doi:10.1103/physrevd.72.072006

Aprile, E., Giboni, K. L., Majewski, P., Ni, K., and Yamashita, M. (2007). Observation of anticorrelation between scintillation and ionization for MeV gamma rays in liquid xenon. *Phys. Rev. B* 76, 014115. doi:10.1103/PhysRevB.76.014115

Aprile, E., Mukherjee, R., and Suzuki, M. (1991). Performance of a liquid xenon ionization chamber irradiated with electrons and gamma-rays. *Nucl. Instrum. Methods Phys. Res. Sect. A Accel. Spectrom. Detect. Assoc. Equip.* 302, 177–185. doi:10.1016/0168-9002(91)90507-M

Arneodo, F., Baiboussinov, B., Badertscher, A., Benetti, P., Bernardini, E., Bettini, A., et al. (2000). Scintillation efficiency of nuclear recoil in liquid xenon. *Nucl. Instrum. Methods Phys. Res. Sect. A Accel. Spectrom. Detect. Assoc. Equip.* 449, 147–157. doi:10.1016/s0168-9002(99)01300-5

Baudis, L. (2018). The search for dark matter. *Eur. Rev.* 26, 70–81. doi:10.1017/S1062798717000783

Baudis, L., Dujmovic, H., Geis, C., James, A., Kish, A., Manalaysay, A., et al. (2013). Response of liquid xenon to Compton electrons down to 1.5 keV. *Phys. Rev. D.* 87, 115015. doi:10.1103/physrevd.87.115015

Baudis, L., Sanchez-Lucas, P., and Thieme, K. (2021). A measurement of the mean electronic excitation energy of liquid xenon. *Eur. Phys. J. C* 81, 1060. doi:10.1140/epjc/s10052-021-09834-x

Berger, M., Coursey, J., Zucker, M., and Chang, J. (2005). "ESTAR, PSTAR, and ASTAR: computer programs for calculating stopping-power and range tables for electrons," in *Protons, and helium ions*. Gaithersburg, MD: National Institute of Standards and Technology.

Bezrukov, F., Kahlhoefer, F., and Lindner, M. (2011). Interplay between scintillation and ionization in liquid xenon dark matter searches. *Astropart. Phys.* 35, 119–127. doi:10.1016/j.astropartphys.2011.06.008

Biekert, A., Chang, C., Fink, C., Garcia-Sciveres, M., Glazer, E., Guo, W., et al. (2022). Scintillation yield from electronic and nuclear recoils in superfluid He-4. *Phys. Rev. D.* 105, 092005. doi:10.1103/physrevd.105.092005

Birks, J. (1964). "The theory and practice of scintillation counting (chapter 8 - organic liquid scintillators)," in *International series of monographs in electronics and instrumentation*. Pergamon. doi:10.1016/B978-0-08-010472-0.50001-X

Bo, Z. (2024). *First indication of solar ^{8}B neutrino flux through coherent elastic neutrino-nucleus scattering in PandaX-4T. arXiv:2407.10892.*

Boulton, E. M., Bernard, E., Destefano, N., Edwards, B., Gai, M., Hertel, S., et al. (2017). Calibration of a two-phase xenon time projection chamber with a ^{37}Ar source. *JINST* 12, P08004. doi:10.1088/1748-0221/12/08/P08004

Bressi, G., Carugno, G., Conti, E., Noce, C., and Iannuzzi, D. (2001). Infrared scintillation: a comparison between gaseous and liquid xenon. *Nucl. Instrum. Methods Phys. Res. Sect. A Accel. Spectrom. Detect. Assoc. Equip.* 461, 378–380. 8th Pisa Meeting on Advanced Detectors. doi:10.1016/S0168-9002(00)01249-3

Caratelli, D. (2022). Low-energy physics in neutrino LArTPCs. *arXiv:2203.00740.*

Chepel, V., and Araújo, H. (2013). Liquid noble gas detectors for low energy particle physics. *J. Instrum.* 8, R04001. doi:10.1088/1748-0221/8/04/r04001

Chepel, V. Y. (1999). "Primary scintillation yield and alpha/beta ratio in liquid xenon," in *Proceedings of the 1999 IEEE 13th international conference on dielectric liquids*, 52.

Conti, E., DeVoe, R., Gratta, G., Koffas, T., Waldman, S., Wodin, J., et al. (2003). Correlated fluctuations between luminescence and ionization in liquid xenon. *Phys. Rev. B* 68, 054201. doi:10.1103/PhysRevB.68.054201

Dahl, C. E. (2009). *The physics of background discrimination in liquid xenon, and first results from XENON10 in the hunt for WIMP dark matter*. Princeton University. Ph.D. thesis.

Davis, C., Hall, C., Albert, J., Barbeau, P., Beck, D., Belov, V., et al. (2016). An optimal energy estimator to reduce correlated noise for the EXO-200 light readout. *JINST* 11, P07015. doi:10.1088/1748-0221/11/07/P07015

Delaquis, S., Jewell, M., Ostrovskiy, I., Weber, M., Ziegler, T., Dalmasson, J., et al. (2018). Deep neural networks for energy and position reconstruction in EXO-200. *J. Instrum.* 13, P08023. doi:10.1088/1748-0221/13/08/p08023

Dobi, A. (2014). *Measurement of the electron recoil band of the LUX dark matter detector with a tritium calibration source.* Maryland U. College Park: Ph.D. thesis. doi:10.13016/M24P5P

Doke, T., Crawford, H. J., Hitachi, A., Kikuchi, J., Lindstrom, P. J., Masuda, K., et al. (1988). LET dependence of scintillation yields in liquid argon. *Nucl. Instrum. Methods Phys. Res. Sect. A Accel. Spectrom. Detect. Assoc. Equip.* 269, 291–296. doi:10.1016/0168-9002(88)90892-3

Doke, T., Hitachi, A., Kikuchi, J., Masuda, K., Okada, H., and Shibamura, E. (2002). Absolute scintillation yields in liquid argon and xenon for various particles. *Jpn. J. Appl. Phys.* 41, 1538–1545. doi:10.1143/jjap.41.1538

Doke, T., Hitachi, A., Kubota, S., Nakamoto, A., and Takahashi, T. (1976). Estimation of Fano factors in liquid argon, krypton, xenon and xenon-doped liquid argon. *Nucl. Instrum. Methods* 134, 353–357. doi:10.1016/0029-554X(76)90292-5

Edwards, B., Bernard, E., Boulton, E., Destefano, N., Gai, M., Horn, M., et al. (2018). Extraction efficiency of drifting electrons in a two-phase xenon time projection chamber. *JINST* 13, P01005. doi:10.1088/1748-0221/13/01/P01005

Faham, C., Gehman, V., Currie, A., Dobi, A., Sorensen, P., and Gaitskell, R. (2015). Measurements of wavelength-dependent double photoelectron emission from single photons in VUV-sensitive photomultiplier tubes. *J. Instrum.* 10, P09010. doi:10.1088/1748-0221/10/09/p09010

Fano, U. (1947). Ionization yield of radiations. II. The fluctuations of the number of ions. *Phys. Rev.* 72, 26–29. doi:10.1103/PhysRev.72.26

Goetzke, L., Aprile, E., Anthony, M., Plante, G., and Weber, M. (2017). Measurement of light and charge yield of low-energy electronic recoils in liquid xenon. *Phys. Rev. D.* 96, 103007. doi:10.1103/physrevd.96.103007

Hitachi, A. (2005). Properties of liquid xenon scintillation for dark matter searches. *Astropart. Phys.* 24, 247–256. doi:10.1016/j.astropartphys.2005.07.002

Horn, M., Belov, V., Akimov, D., Araújo, H., Barnes, E., Burenkov, A., et al. (2011). Nuclear recoil scintillation and ionisation yields in liquid xenon from ZEPLIN-III data. *Phys. Lett. B* 705, 471–476. doi:10.1016/j.physletb.2011.10.038

Huang, D. (2020). *Ultra-low energy calibration of the LUX and LZ dark matter detectors*. Brown U: Ph.D. thesis. doi:10.26300/zvs6-fx07

James, R., Palmer, J., Kaboth, A., Ghag, C., and Aalbers, J. (2022). FlameNEST: explicit profile likelihoods with the Noble Element Simulation Technique. *J. Instrum.* 17, P08012. doi:10.1088/1748-0221/17/08/p08012

Lenardo, B., Kazkaz, K., Manalaysay, A., Mock, J., Szydagis, M., and Tripathi, M. (2015). A global analysis of light and charge yields in liquid xenon. *IEEE Trans. Nucl. Sci.* 62, 3387–3396. doi:10.1109/TNS.2015.2481322

Lenardo, B., Xu, J., Pereverzev, S., Akindele, O. A., Naim, D., Kingston, J., et al. (2019). Measurement of the ionization yield from nuclear recoils in liquid xenon between 0.3 – 6 keV with single-ionization-electron sensitivity. *arXiv:1908.00518*. doi:10.48550/arXiv.1908.00518

Lin, Q., Fei, J., Gao, F., Hu, J., Wei, Y., Xiao, X., et al. (2015). Scintillation and ionization responses of liquid xenon to low energy electronic and nuclear recoils at drift fields from 236 V/cm to 3.93 kV/cm. *Phys. Rev. D.* 92, 032005. doi:10.1103/PhysRevD.92.032005

Lindhard, J. (1963). Range concepts and heavy ion ranges. *Mat. Fys. Medd. K. Dan. Vidensk. Selsk.* 33, 10.

Manzur, A., Curioni, A., Kastens, L., McKinsey, D., Ni, K., and Wongjirad, T. (2010). Scintillation efficiency and ionization yield of liquid xenon for mono-energetic nuclear recoils down to 4 keV. *Phys. Rev. C* 81, 025808. doi:10.1103/PhysRevC.81.025808

McMonigle, R. (2024). Updating nuclear recoil models in the Noble Element Simulation Technique for the LUX-ZEPLIN experiment. Ph.D. thesis, UAlbany SUNY.

Mei, D. M., Yin, Z. B., Stonehill, L., and Hime, A. (2008). A model of nuclear recoil scintillation efficiency in noble liquids. *Astropart. Phys.* 30, 12–17. doi:10.1016/j.astropartphys.2008.06.001

Mozumder, A. (1995). Free-ion yield in liquid argon at low-LET. *Chem. Phys. Lett.* 238, 143–148. doi:10.1016/0009-2614(95)00384-3

Mu, W., and Ji, X. (2015). Ionization yield from nuclear recoils in liquid-xenon dark matter detection. *Astropart. Phys.* 62, 108–114. doi:10.1016/j.astropartphys.2014.07.013

Mu, W., Xiong, X., and Ji, X. (2015). Scintillation efficiency for low energy nuclear recoils in liquid xenon dark matter detectors. *Astropart. Phys.* 61, 56–61. doi:10.1016/j.astropartphys.2014.06.010

Nygren, D. R. (2013). Columnar recombination: a tool for nuclear recoil directional sensitivity in a xenon-based direct detection WIMP search. *J. Phys. Conf. Ser.* 460, 012006. doi:10.1088/1742-6596/460/1/012006

Obodovskii, I., and Ospanov, K. (1994). Scintillation output of liquid xenon for low-energy gamma-quanta. *Instrum. Exp. Tech.* 37, 42–45.

Piazza, O., Velan, V., and McKinsey, D. (2025). A first principles approach to e-ion recombination in liquid Xe. *To be published* .

Plante, G. (2012). The XENON100 dark matter experiment: design, construction, calibration and 2010 search results with improved measurement of the scintillation response of liquid xenon to low-energy nuclear recoils. *Ph.D. thesis, Columbia U. (main).*

Plante, G., Aprile, E., Budnik, R., Choi, B., Giboni, K. L., Goetzke, L. W., et al. (2011). New measurement of the scintillation efficiency of low-energy nuclear recoils in liquid xenon. *Phys. Rev. C* 84, 045805. doi:10.1103/physrevc.84.045805

Platzman, R. L. (1961). Total ionization in gases by high-energy particles: an appraisal of our understanding. *Int. J. Appl. Radiat. Isotopes* 10, 116–127. doi:10.1016/0020-708x(61)90108-9

Rischbieter, G. R. C. (2022). Signal yields and detector modeling in xenon time projection chambers, and results of an effective field theory dark matter search using LUX data. *Ph.D. thesis, UAlbany SUNY*.

Rutkai, G., Thol, M., Span, R., and Vrabec, J. (2017). How well does the Lennard-Jones potential represent the thermodynamic properties of noble gases? *Mol. Phys.* 115, 1104–1121. doi:10.1080/00268976.2016.1246760

Sarkis, Y., Aguilar-Arevalo, A., and D'Olivo, J. C. (2020). Study of the ionization efficiency for nuclear recoils in pure crystals. *Phys. Rev. D.* 101, 102001. doi:10.1103/PhysRevD.101.102001

Sorensen, P. (2011a). Lowering the low-energy threshold of xenon-based detectors. *Proc. Identif. Dark Matter 2010 — PoS(IDM2010)*, 017. doi:10.22323/1.110.0017

Sorensen, P. (2011b). Anisotropic diffusion of electrons in liquid xenon with application to improving the sensitivity of direct dark matter searches. *Nucl. Instrum. Methods Phys. Res. Sect. A Accel. Spectrom. Detect. Assoc. Equip.* 635, 41–43. doi:10.1016/j.nima.2011.01.089

Sorensen, P. (2015). Atomic limits in the search for galactic dark matter. *Phys. Rev. D.* 91, 083509. doi:10.1103/PhysRevD.91.083509

Sorensen, P., and Dahl, C. E. (2011). Nuclear recoil energy scale in liquid xenon with application to the direct detection of dark matter. *Phys. Rev. D.* 83, 063501. doi:10.1103/PhysRevD.83.063501

Sorensen, P., Manzur, A., Dahl, C., Angle, J., Aprile, E., Arneodo, F., et al. (2009). The scintillation and ionization yield of liquid xenon for nuclear recoils. *Nucl. Instrum. Methods Phys. Res. Sect. A Accel. Spectrom. Detect. Assoc. Equip.* 601, 339–346. doi:10.1016/j.nima.2008.12.197

Szydagis, M. (2020). NEST: Noble Element Simulation Technique, A symphony of scintillation. Available at: http://nest.physics.ucdavis.edu.

Szydagis, M., Barry, N., Kazkaz, K., Mock, J., Stolp, D., Sweany, M., et al. (2011). NEST: a comprehensive model for scintillation yield in liquid xenon. *JINST* 6, P10002. doi:10.1088/1748-0221/6/10/p10002

Szydagis, M., Block, G. A., Farquhar, C., Flesher, A. J., Kozlova, E. S., Levy, C., et al. (2021a). A review of basic energy reconstruction techniques in liquid xenon and argon detectors for dark matter and neutrino physics using NEST. *Instruments* 5, 13. doi:10.3390/instruments5010013

Szydagis, M., Balajthy, J., Block, G. A., Brodsky, J. P., Cutter, J. E., Farrell, S. J., et al. Noble Element Simulation Technique (2022). doi:10.5281/zenodo.6989015

Szydagis, M., Fyhrie, A., Thorngren, D., and Tripathi, M. (2013). Enhancement of NEST capabilities for simulating low-energy recoils in liquid xenon. *JINST* 8, C10003. doi:10.1088/1748-0221/8/10/C10003

Szydagis, M., Levy, C., Blockinger, G., Kamaha, A., Parveen, N., and Rischbieter, G. (2021b). Investigating the XENON1T low-energy electronic recoil excess using NEST. *Phys. Rev. D.* 103, 012002. doi:10.1103/PhysRevD.103.012002

Tan, A., Xiao, M., Cui, X., Chen, X., Chen, Y., Fang, D., et al. (2016). Dark matter results from first 98.7 Days of data from the PandaX-II experiment. *Phys. Rev. Lett.* 117, 121303. doi:10.1103/PhysRevLett.117.121303

Thomas, J., and Imel, D. A. (1987). Recombination of electron-ion pairs in liquid argon and liquid xenon. *Phys. Rev. A* 36, 614–616. doi:10.1103/PhysRevA.36.614

Thomas, J., Imel, D. A., and Biller, S. (1988). Statistics of charge collection in liquid argon and liquid xenon. *Phys. Rev. A* 38, 5793–5800. doi:10.1103/PhysRevA.38.5793

Wang, L., and Mei, D. M. (2017). A comprehensive study of low-energy response for xenon-based dark matter experiments. *J. Phys. G Nucl. Part. Phys.* 44, 055001. doi:10.1088/1361-6471/aa6403

Westerdale, S. (2024). The DEAP-3600 liquid argon optical model and NEST updates. *JINST* 19, C02008. doi:10.1088/1748-0221/19/02/C02008

Xu, J., Pereverzev, S., Lenardo, B., Kingston, J., Naim, D., Bernstein, A., et al. (2019). Electron extraction efficiency study for dual-phase xenon dark matter experiments. *Phys. Rev. D.* 99, 103024. doi:10.1103/PhysRevD.99.103024

Yamashita, M., Doke, T., Kawasaki, K., Kikuchi, J., and Suzuki, S. (2004). Scintillation response of liquid Xe surrounded by PTFE reflector for gamma rays. *Nucl. Instrum. Methods Phys. Res. Sect. A Accel. Spectrom. Detect. Assoc. Equip.* 535, 692–698. doi:10.1016/j.nima.2004.06.168

Yan, B., Abdukerim, A., Chen, W., Chen, X., Chen, Y., Cheng, C., et al. (2021). Determination of responses of liquid xenon to low energy electron and nuclear recoils using a PandaX-II detector. *Chin. Phys. C* 45, 075001. doi:10.1088/1674-1137/abf6c2